ZESZYTY NAUKOWE
POLITECHNIKI RZESZOWSKIEJ

SCIENTIFIC LETTERS
OF RZESZOW UNIVERSITY OF TECHNOLOGY

NR 293

(e-ISSN 2300-5211)

MECHANIKA

Kwartalnik
tom XXXIII
zeszyt 88 (nr 3/2016)
lipiec-wrzesień

WYDZIAŁ
BUDOWY MASZYN
I LOTNICTWA
POLITECHNIKI RZESZOWSKIEJ

Wydano za zgodą Rektora

p-ISSN 0209-2689
e-ISSN 2300-5211

Wersja drukowana Kwartalnika jest wersją pierwotną.

Redakcja czasopisma: Politechnika Rzeszowska, Wydział Budowy Maszyn i Lotnictwa
al. Powstańców Warszawy 8, 35-959 Rzeszów (e-mail: tomtrz@prz.edu.pl)
http://oficyna.portal.prz.edu.pl/pl/zeszyty-naukowe/mechanika

Wydawca: Oficyna Wydawnicza Politechniki Rzeszowskiej
al. Powstańców Warszawy 12, 35-959 Rzeszów (e-mail:oficyna1@prz.edu.pl)
http://oficyna.portal.prz.edu.pl
Informacje dodatkowe i stopka – str. 267

SPIS TREŚCI

ZESZYTY NAUKOWE POLITECHNIKI RZESZOWSKIEJ 293, Mechanika 88
RUTMech, t. XXXIII, z. 88 (3/16), lipiec-wrzesień 2016, s. 189-197

Ivan GAJDOŠ[1]
Emil SPIŠÁK[2]
Tomasz JACHOWICZ[3]
Tomasz GARBACZ[4]

TENSILE PROPERTIES OF ADDITIVELY MANUFACTURED POLYETHERIMIDE PARTS

This paper presents the results of a study of evaluating the influence of path generation strategy on tensile properties of samples made by additive manufacturing technology FDM (Fused Deposition Modeling). Several scientific studies were focused on the influence of path generation strategy on mechanical properties of deposited material. ABS and PLA are the most investigated materials used in FDM. This paper is aimed to determine the influence of selected path generation strategies on tensile strength of parts fabricated with ULTEM 9085 thermoplastic. The results obtained in experiments confirmed that proposed path generation strategy allowed to increase tensile strength by 25% compared to a situation when the samples were fabricated with default path generation setting.

Keywords: fused deposition modeling, tensile test, polyetherimide

1. Introduction

Nowadays, fused deposition modelling (FDM) and fused filament fabrication (FFF) are one of the most used additive manufacturing (AM) techniques due to its ability to manufacture parts with very complex geometries at relatively low prices. The main reasons for the growing popularity of AM techniques are their reliability, safe and simple fabrication process, low cost of material, and the availability to processing a variety of thermoplastics. The major research problem is to balance the ability to produce both tough and aesthetically pleasing products with their functionality.

---

[1] Autor do korespondencji/corresponding author: Ivan Gajdoš, Technical University of Košice, Mäsiarska 74, 040 01 Košice, Slovakia, e-mail: ivan.gajdos@tuke.sk

[2] Emil Spišák,Technical University of Košice, Mäsiarska 74, 040 01 Košice, Slovakia, e-mail: emil.spisak@tuke.sk

[3,4] Tomasz Jachowicz, Tomasz Garbacz, Politechnika Lubelska, e-mails: t.jachowicz@pollub.pl, t.garbacz@pollub.pl

In the FDM process, the material is initially in the raw form of a flexible filament. The filament is then partially heated above the melting (glass transition) temperature and extruded through a heated nozzle. The extrusion process is mostly conducted in environment with a controlled temperature. In lw cost systems instead of temperature controlled environment a heated platform is used. The material is extruded in a thin layer onto the building platform (first layer) or onto the previously built model layer on the building platform in the form of a prescribed two-dimensional (x-y) layer pattern (fig. 1). The deposited material cools, solidifies, and bonds with adjoining material. After an entire layer is deposited, the build platform moves downward along the z-axis by an increment equal to the filament height (layer thickness) and the next layer is deposited on the top of it. The platen or table on which the build sheet is placed lies in the x-y plane.

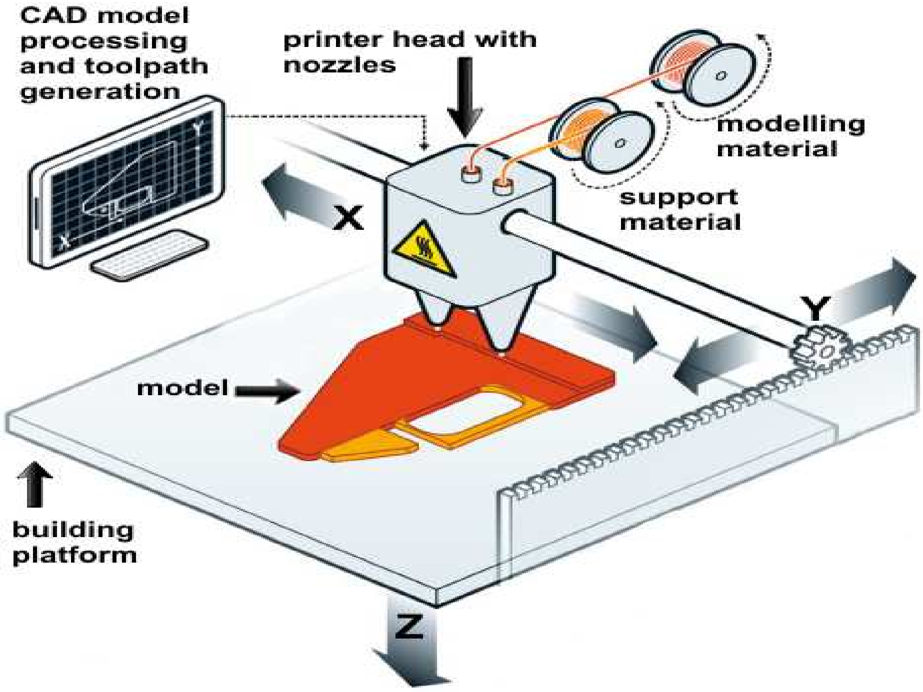

Fig. 1. Scheme of fused deposition modelling (FDM) process

Low cost or budget FFF systems are equipped only with one nozzle, and the supporting structure is fabricated with the same material as a model itself. This makes the support removal difficult for the operator. Mid-range and high level FDM systems generally come with two nozzles, one for model material and one for support material. Different properties of support material, cause lower interbond strength between model/support interface and thus easier to remove support structures after the model is built. Nowadays a wide variety of thermoplastics materials in a form of virgin materials, blends and composites are available for the FFF applications. Although AM is an efficient technology, full scale application has not gained much attention because of compatibility of presently available materials with AM technologies [1]. AM offers design and environmental advantages over classical manufacturing processes, the adoption of AM as a means for fabricating end-use components has been delayed by the technologies' narrow selection of available materials. The biggest part of materials used by modern AM technologies are polymers. There are also possibilities to use some metals (such as steel alloys and titanium) and ceramics. While there are presently available different types of polymeric materials that can be used in AM, the material properties are typically not as strong as their conventionally manufactured counterparts due to the anisotropy resulting from the layer-by-layer nature of the AM process [2].

AM is generally able to help to design and speed up the whole process of product development especially in the case when producing very complicated parts which production using traditional manufacturing methods would be challenging or even impossible. Designers use the possibility of design freedom to integrate function of several parts into one product. Pre-processing phase in interaction between CAD and AM system is mostly relatively seamless and there is less or no concern about interpretation of the design intent. AM system reduces lot of steps or stages necessary in the case of traditional manufacturing processes[3].

Manufacturing of complex shaped AM products with good aesthetically appealing with actually available AM technologies is not challenging. The problem is to produce AM parts that are functionally reliable, especially when building parts with geometry details on the edge of AM system resolution. Another issue is the inhomogeneity of mechanical properties caused by the nature of the layered manufacturing. This phenomenon had to be taken into account, when designing AM product, and is well known also in FDM technology. Lots of research studies results present the relationship between process setting conditions (raster angle, raster gap, deposition strategy, temperature, etc.) and the resulting mechanical properties[4-6]. These results show that the FDM produced parts are the most vulnerable when they are loaded in the z-building direction.

Although FDM is a very widespread technology, the manufacturer's policy often causes material incompatibly between individual FDM machines. Research studies mentioned above, solved the issue of mechanical properties for parts made of ABS, PLA or polycarbonate, which are the most commonly used materials in FDM technology. The presented study focuses on relatively rare used material in FDM technology ULTEM9085® supplied by Stratasys® (general polymer classification is polyetherimide - PEI). The goal of investigations was to determine one of the mechanical properties, namely tensile strength of FDM fabricated part. The part was produced under system`s default path generation strategy (PGS) and under proposed alternative strategy with an intention to minimize air gaps in the volume of the part. Alternative path generation strategy was adapted to specific conditions applicable for ULTEM 9085 in Insight® 9.1 software. PGS is based on findings of Gajdoš et al. [7] who investigated samples made of polycarbonate, where the distribution of air gaps in the sample structure was not random. The structure of prepared samples was modified by locating air gaps in one part of the samples volume, thus significantly affecting tensile strength of the sample. The location of the air gaps in the volume is associated with the start point of layer raster forming (fig. 2).

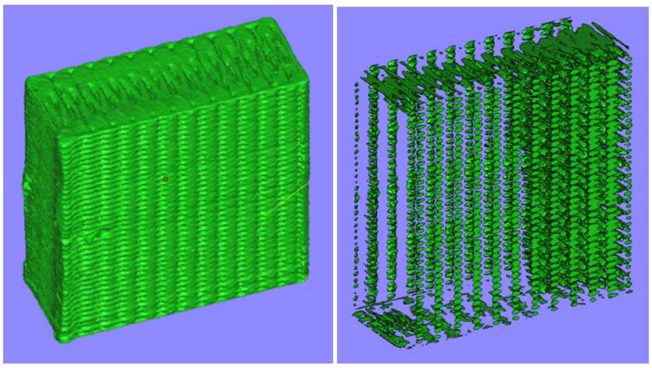

Fig. 2. Metrotomography 3D scanned FDM sample (left) and location of air gaps in the sample (right)

2. Experimental procedure

In this study, the samples made of ULTEM 9085 were prepared using Fortus 400mc® production system. Path generation strategy in pre-processing stage of the fabrication process was determined in Insight® 9.1 software. The dimensions of the samples were in accordance with STN ISO 527-2 (fig. 3). All the samples were fabricated with orientation as presented in figure 4.

This direction is recognized as the weakest for strength of FDM parts. The samples were prepared directly from prepared 3D STL model (dimensions are shown in figure 3) under the default setting of parameters values and slicing layer height of 0.254 mm. Three types of path generation strategy were used with a raster angle of 45°, 90° raster angle between the following layers with a raster air gap of 0 mm and a raster width of 0.508 mm. The samples differed only in the number of outlines (fig. 4).

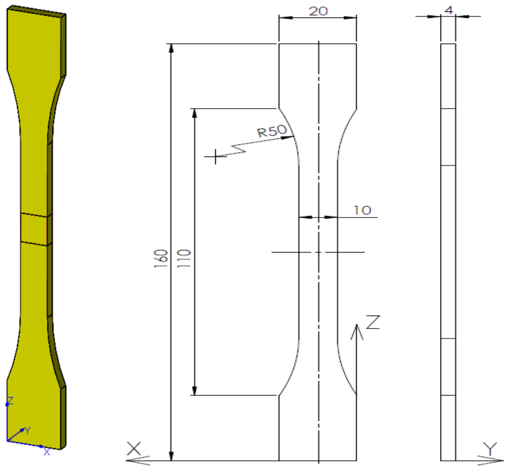

Fig. 3. Tensile test specimen dimensions, building orientation

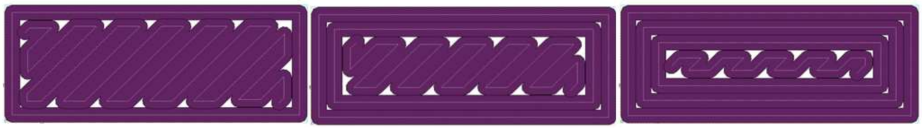

Fig. 4. Tensile test specimens default path generation strategy with one (left), two (middle) and three (right) outlines

Preparing samples with alternative path generation strategy required to modify designing and pre-processing procedures. There were some knowledge and software limitations which have been discussed in previous study [7]. As mentioned above, the cross-section area of the tensile test sample is relatively small, and consequently appearing fiber deposition leads to inhomogeneous air gap distribution (fig. 2). To avoid this phenomenon a plate was designed with the following dimensions: a thickness of 4 mm, a height of 160 mm, and a width of 100mm. Final shape of the test samples was machined on the milling machine.

Actual raster width setting and path generation strategy in Insight® 9.1 for ULTEM 9085 and layer height of 0.254 mm do not allow to prepare desired alternative deposition strategy as shown in figure 5. Available raster widths cannot create combination of outline raster with 50% width of internal raster. Thus, the raster deposition strategy without outline was adopted and the desired offset between layers was obtained by modeling of layer offset directly in CAD model. Final path generation strategy setup was as follows: no outline, a raster width of 0.5 mm, a raster angle of 0° and a raster angle between layers of 180°. Five specimens were prepared for all types of samples used in the experiment which are listed in table 1.

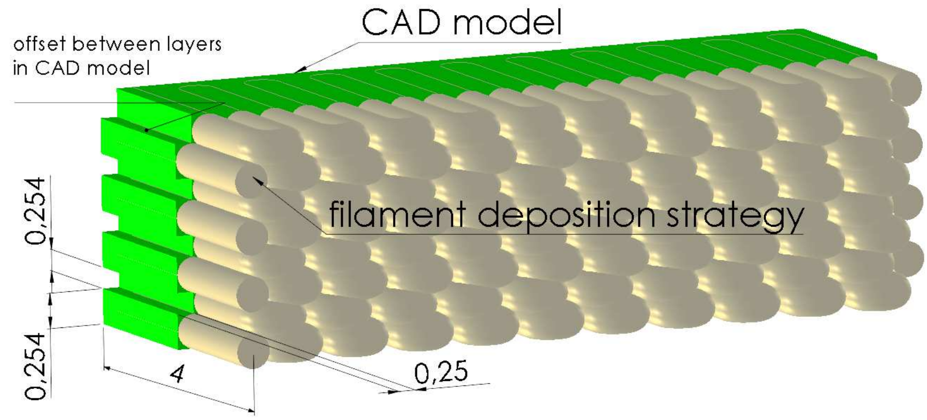

Fig. 5. CAD model of plate cross-section (green) and alternative filament deposition strategy

Table 1. Path generation strategies used in experiments

Sample type	Raster width [mm]	Raster angle [°]	Raster angle between following layers [°]	Number of outline contours	Width of outline contours [mm]
A	0.508	45	90	1	0.508
B	0.508	45	90	2	0.508
C	0.508	45	90	3	0.508
D	0.500	0	180	0	-

3. Results and discussion

The average values of ultimate tensile strength for all types of samples are presented in figure 6. The tensile strength value for the sample “A” prepared with default settings was 36.64 MPa. Increasing of the number of outlines, decreases the resulting tensile strength to 34.71 MPa in the case of the sample “ B” and to 30.95 MPa in the case of the sample “C”. Increasing of the number of outlines has negative influence on resulting tensile strength. The highest tensile strength was measured for “D” samples, made with alternative path generation strategy. Average value of 46.04 MPa means improvement of tensile strength by 25.56%, when compared with tensile strength of the sample “A”.

In the figure 7 stress-elongation curves of selected samples determined through tensile tests are presented. Observed elongation at break for sample “D”is 3.14 mm. Compared to other samples (2.12-2.23 mm) the elongation value is higher of about 40.08-48.11%. It is assumed that the high layer to layer bond strength, allows utilizing bigger portion of filament elastic deformation capacity.

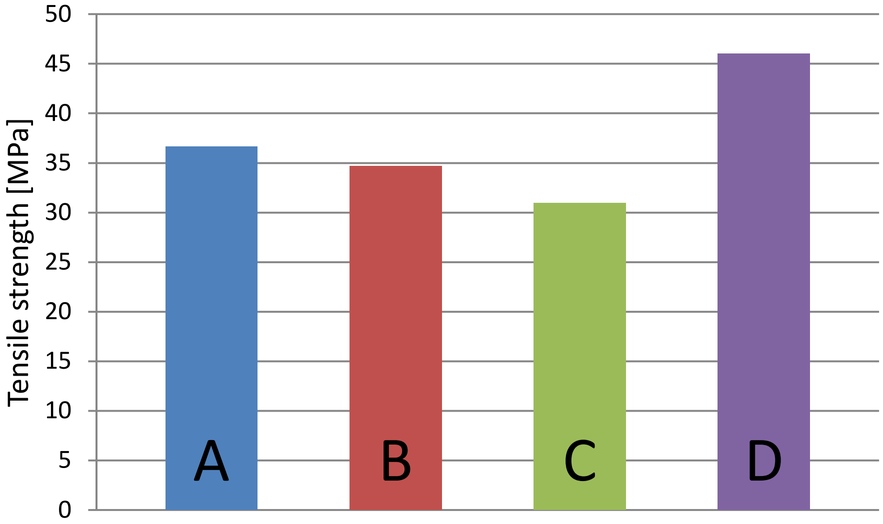

Fig. 6. Average tensile strength for all sample types

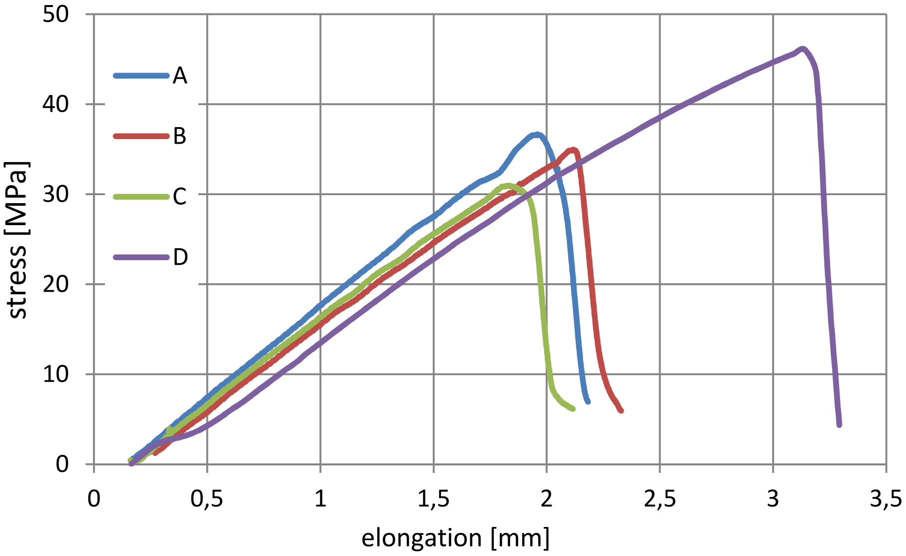

Fig. 7. Stress-elongation curves of tested samples determined through tensile tests

4. Conclusions

AM is able to help to design and speed up the whole process of product development, especially in the case when producing very complicated parts. Designers use the possibility of design freedom to integrate function of several parts into one product. The inhomogeneity of mechanical properties caused by the nature of the layered manufacturing is a main problem in AM products. This phenomenon had to be taken into account, when designing AM product, and is also well known in FDM technology. Generating a path deposition strategy for FDM parts with default settings causes fabrication of parts with relatively high amount of voids in the structure. The proposed alternative path generation strategy, had led to increasing of tensile strength by 26.56% and also increasing of elongation at break by 40.08%. However, at this moment there are several challenges that have to be solved to apply this strategy when manufacturing FDM parts. Among others, actual slicing and path generating software do not incorporate into the developed alternative part generation strategy. In this study, the path generation is adopted in manually designed CAD model. For complex shaped parts this strategy would be nearly impossible, or very time consuming. The second problem is the inhomogeneity of air-gaps distribution, which was solved in this study by printing the plate followed by machining of the samples. For practical purposes this is not applicable. Decreasing the surface quality of FDM parts is another drawback of proposed path generation strategy.

Acknowledgement

Authors are grateful for the support of experimental works by project VEGA no. 1/0872/14

References

[1] Levy G. N., Schindel R., Kruth J. P.: Rapid manufacturing and rapid tooling with layer manufacturing (LM) technologies, state of the art and future perspectives, CIRP Annals: Manuf. Technol., 52 (2003) 589-609.

[2] Ivanova O., Williams C., Campbell T.: Additive manufacturing (AM) and nanotechnology: promises and challenges, Rapid Prototyping J., 19 (2013) 353-364.

[3] Gibson I., Rosen D. W., Stucker B.: Additive Manufacturing Technologies: Rapid Prototyping to Direct Digital Manufacturing, Springer, Heidelberg 2010.

[4] C. Onwubolu G., Rayegani F.: Characterization and optimization of mechanical properties of abs parts manufactured by the fused deposition modelling process, Int. J. Manuf. Eng., vol. 2014, Article ID 598531.

[5] Lipina J., Krys V., Sedlák J.: Shaped glued connection of two parts made by rapid prototyping technology, Appl. Mech. Mat., 2014, 541, 978-3-03835-111-5

[6] Sood A.K, Ohdar R.K., Mahapatra S.S.: Parametric appraisal of mechanical property of fused deposition modelling processed parts, Materials and Design, 2010, 287, 0264-1275.

[7] Gajdoš I., Slota J., Spišák E., Jachowicz T., Tor-Swiatek A.: Structure and tensile properties evaluation of samples produced by Fused Deposition Modeling, Open Engeneering 2016; 6:86-89, DOI 10.1515/eng-2016-0011.

WŁAŚCIWOŚCI MECHANICZNE PRZY ROZCIĄGANIU CZĘŚCI Z POLIETEROIMIDU WYTWARZANYCH W TECHNOLOGII PRZYROSTOWEJ

Streszczenie

W artykule przedstawiono wyniki badań oceniających, w próbie rozciągania, wpływ strategii generowania ścieżki na właściwości mechaniczne próbek wytworzonych w technologii osadzania topionego materiału (ang. FDM - Fused Deposition Modeling). Liczne badania naukowe były skupione na wpływie strategii generowania ścieżki na właściwości mechaniczne materiału osadzanego. Najczęściej badanymi materiałami stosowanymi w technologii FDM są ABS oraz PLA. Celem niniejszego artykułu określenie wpływu wybranych strategii generowania ścieżki na wytrzymałość na rozciąganie elementów wytworzonych z termoplastu ULTEM9085. Wyniki badań eksperymentalnych potwierdziły, że proponowana strategia wytwarzania ścieżki pozwoliła zwiększyć wytrzymałość na rozciąganie o 25% w porównaniu z sytuacją, gdy próbki były wytwarzane przy użyciu domyślnych ustawień generacji ścieżki.

Słowa kluczowe: osadzanie topionego materiału, próba rozciągania, polieteroimid

DOI: 10.7862/rm.2016.15

Otrzymano/received: 24.05.2016 r.
Zaakceptowano/accepted: 14.07.2016 r.

ZESZYTY NAUKOWE POLITECHNIKI RZESZOWSKIEJ 293, Mechanika 88
RUTMech, t. XXXIII, z. 88 (3/16), lipiec-wrzesień 2016, s. 199-212

Piotr GIERLAK[1]

ANALIZA WIĘZÓW MANIPULATORA W ZADANIU ZROBOTYZOWANEJ OBRÓBKI MECHANICZNEJ DYFUZORA

Artykuł dotyczy analizy więzów geometrycznych narzuconych na końcówkę roboczą robota manipulacyjnego, którego zadaniem jest realizacja obróbki mechanicznej dyfuzora. Z punktu widzenia teorii sterowania, realizacja omawianego zadania jest traktowana jako sterowanie obiektem z ograniczeniami ruchu. Wymaga to określenia zadanej trajektorii układu sterowania robota rozumianej jako trajektoria pozycyjna oraz siłowa. W pracy zaprezentowano geometrię dyfuzora wraz z opisem matematycznym krawędzi, która ma zostać zatępiona. Podano zestaw więzów naturalnych i sztucznych, pozycyjnych i siłowych dla tego zadania oraz dla zadania wiercenia otworów. Podano sposób wyznaczania trajektorii pozycyjnej i siłowej, która będzie stanowić trajektorię zadaną układu sterowania robota. Zaprezentowano wyniki symulacji generowania trajektorii ruchu końcówki roboczej.

Słowa kluczowe: więzy geometryczne, robot manipulacyjny, planowanie trajektorii, zrobotyzowana obróbka

1. Wprowadzenie

Poprawna realizacja obróbki mechanicznej elementów części maszyn i urządzeń wymaga zastosowania precyzyjnych stanowisk obróbczych, najczęściej maszyn CNC. Specyfika niektórych zadań obróbki, związana z niepewnością położenia oraz kształtu obrabianej powierzchni czy krawędzi powoduje, że niektóre operacje są często wykonywane ręcznie na stanowiskach ślusarskich czy wiertarskich. Automatyzacja takich operacji jest możliwa, wymaga jednak zastosowania złożonych systemów, których istotną cechą jest programowalność i elastyczność [2]. W skład takich systemów wchodzą przede wszystkim roboty z odpowiednimi narzędziami do obróbki mechanicznej oraz inne urządzenia pomocnicze takie jak pozycjonery, transportery i systemy wizyjne [3].

Takie systemy umożliwiają zaprogramowanie i realizację procesów ob-

---

[1] Autor do korespondencji/corresponding author: Piotr Gierlak, Politechnika Rzeszowska, al. Powstańców Warszawy 12, 35-959 Rzeszów, tel.: (17) 8651854, e-mail: pgierlak@prz.edu.pl

róbki mechanicznej elementów, których kształt i położenie są zmienne w określonych granicach. Przykładem jest zadanie obróbki mechanicznej dyfuzora silnika (rys. 1). Losowa zmienność kształtu i położenia dyfuzora, który jest elementem odlewu, wynika m.in. ze zjawiska skurczu występującego podczas krzepnięcia oraz niedokładności wykonania formy odlewniczej.

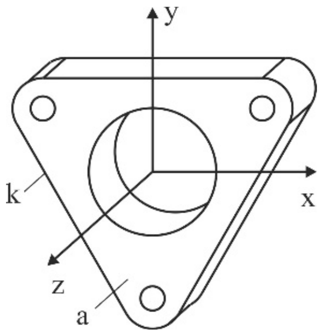

Rys. 1. Kształt dyfuzora

Fig. 1. The shape of the diffuser

Płaszczyzna *a* dyfuzora jest obrobiona przez frezowanie, natomiast krawędź *k* należy zatępić. Ponadto należy wykonać otwory przelotowe o osiach prostopadłych do płaszczyzny *a*.

Ważnym aspektem praktycznym jest wybór sposobu realizacji omówionych zadań. Do realizacji procesu obróbki krawędzi dyfuzora w praktyce można stosować co najmniej dwie strategie sterowania. Pierwsza z nich polega na zastosowaniu tzw. hybrydowego sterowania pozycyjno-siłowego. Hybrydowy sterownik pozycyjno-siłowy [4, 12] powinien umożliwiać:

- sterowanie pozycją końcówki manipulatora wzdłuż kierunków, na których istnieją naturalne więzy siłowe,
- sterowanie siłami wywieranymi przez końcówkę manipulatora wzdłuż kierunków, na których istnieją naturalne więzy pozycyjne,
- realizację dowolnej kombinacji powyższych zadań wzdłuż ortogonalnych kierunków układu więzów $\{c\}$.

Zastosowanie takiej strategii wymaga wyposażenia robota w pakiet sprzętowo-programowy, w skład którego musi wchodzić układ umożliwiający wyznaczenie sił i momentów w końcówce roboczej manipulatora. Można zastosować np. czujnik sił i momentów umieszczony w końcówce robota [2] lub układ pomiaru obciążenia napędów robota [18]. Dodatkowo rozbudowany musi zostać układ sterowania robota w celu realizacji pętli sterowania siłami. Schemat układu sterowania pozycyjno-siłowego umożliwiającego realizację omawianego zadania przedstawiono na rys. 2.

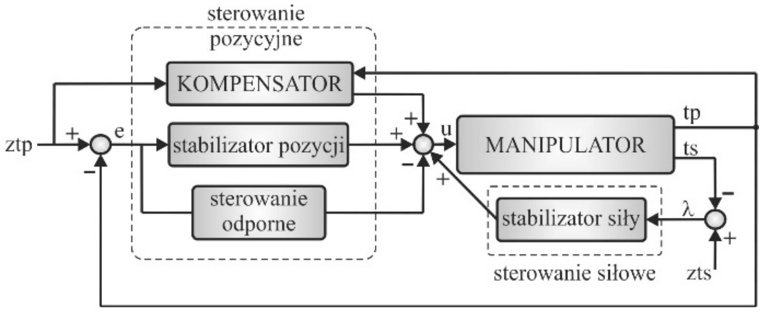

Rys. 2. Schemat układu sterowania pozycyjno-siłowego: ztp - zadana trajektoria pozycyjna, tp - trajektoria pozycyjna, e - błąd realizacji trajektorii pozycyjnej, zts - zadana trajektoria siłowa, ts - trajektoria siłowa, λ - błąd realizacji trajektorii siłowej, u - sterowanie

Fig. 2. The scheme of the position/force control system: ztp - desired positional trajectory, tp - positional trajectory, e - error of position, zts - desired force trajectory, ts - force trajectory, λ - error of force, u - control input

Struktura sterowania pozycyjnego jest typowa dla układów sterowania współczesnych robotów, w których problem nadążania za zadaną trajektorią ruchu jest definiowany jako zadanie stabilizacji błędu nadążania. Rolą kompensatora jest kompensowanie nieliniowości sterowanego obiektu, natomiast rolą stabilizatora jest eliminowanie błędu nadążania wynikającego z niedokładnej kompensacji nieliniowości. Dodatkowo wprowadza się człon zapewniający odporność na zakłócenia nazywany sterowaniem odpornym, a jego struktura zależy m.in. od struktury kompensatora i sposobu analizy stabilności układu. Typowym rozwiązaniem stosowanym w pętli sterowania siłowego jest zastosowanie stabilizatora siły, którego celem jest eliminowanie błędu trajektorii siłowej. Szczegółowe opracowania dotyczące rozwiązań stosowanych w układach sterowania pozycyjno-siłowego zostały przedstawione w pracach autora. Analizowano w nich m.in. zastosowanie metod klasycznych, układów neuronowych i neuronowo-rozmytych w sterowaniu pozycyjnym [6, 7, 9, 10] oraz regulatorów konwencjonalnych (PID) i rozmytych w sterowaniu siłowym [11]. Inne rozwiązania sterowania siłowego przedstawione są w pracach [15, 16].

Alternatywnym i tańszym rozwiązaniem, nie wymagającym stosowania układu sterowania siłowego, jest wyposażenie robota manipulacyjnego w tzw. podatne narzędzie [2]. Jest ono tak skonstruowane, że wrzeciono, w którym zamocowane jest narzędzie skrawające, ma możliwość odchylania się od położenia neutralnego. Dostępne na rynku tego typu rozwiązania to np. narzędzia: FDB firmy Schunk [20] oraz DT-A390 firmy RAD [19]. Istota tych rozwiązań polega na sterowaniu podatnością wrzeciona poprzez zmianę ciśnienia powietrza doprowadzanego do narzędzia. Przy większym ciśnieniu powietrza siła wymagana do wychylenia wrzeciona jest większa. Układ taki nie umożliwia sterowania siłami interakcji w torze zamkniętym - stosowane jest tu jedynie sterowanie typu pozycyjnego - a siła interakcji jest dobierana w sposób przybliżony i zależy od aktualnej wartości ciśnienia doprowadzanego do układu sterowania podatnością. Dodatkową korzyścią z zastosowania podatnego narzędzia jest zabezpieczenie robota i obrabianego przedmiotu przed uszkodzeniem w wyniku wygenerowania zbyt dużych sił lub momentów sił.

Obydwie przedstawione strategie sterowania zapewniają kontakt narzędzia z obrabianym przedmiotem nawet wówczas, gdy jego kształt i położenie odbiegają od nominalnych wartości. Jest to efektem uwzględniania w procesie sterowania siły interakcji robota z otoczeniem.

Do wykonania przedstawionych zadań zastosowany zostanie manipulator kartezjański własnej konstrukcji posiadający trzy stopnie swobody [8]. Jest to manipulator przeznaczony do realizacji badań dotyczących m.in. robotyzacji procesów obróbki mechanicznej. Umożliwia on realizowanie dwóch niezależnych translacji końcówki w płaszczyźnie poziomej i jednej w kierunku pionowym. Wyposażony jest w moduły liniowe, w skład których wchodzą prowadnice z wózkami napędzanymi przez silniki prądu stałego za pośrednictwem przekładni zębatych oraz śrub kulowych. W celu umożliwienia realizacji pętli sterowania pozycyjnego manipulator wyposażono w enkodery zamocowane na wałach silników napędowych. Aby umożliwić realizację pętli sterowania siłowego, koniecznej do sterowania siłami interakcji robota z otoczeniem, w końcówce roboczej umieszczono czujnik siły FTD-Gamma SI-130-10 firmy ATI [17]. Jest to czujnik umożliwiający pomiar trzech składowych siły i trzech składowych momentu siły w końcówce roboczej. Do czujnika siły mocowana jest głowica, w której znajduje się narzędzie skrawające, np. pilnik, frez itp.

Z punktu widzenia teorii sterowania robotami, realizacja omawianego zadania jest traktowana jako sterowanie obiektem z częściowymi ograniczeniami ruchu, co prowadzi do sterowania typu pozycyjno-siłowego [16]. Wymaga to określenia zadanej trajektorii układu sterowania robota rozumianej jako trajektoria pozycyjna oraz trajektoria siłowa. Problem ten zostanie wyjaśniony w kolejnych rozdziałach artykułu

W rozdziale 2 przedstawiono więzy manipulatora wynikające z zadania obróbki krawędzi dyfuzora. W rozdziale 3 wyznaczono trajektorię pozycyjno-siłową zgodną z więzami manipulatora. Rozdział 4 dotyczy analizy więzów manipulatora wynikających z zadania wiercenia otworów w dyfuzorze. W ostatnim rozdziale dokonano podsumowania pracy.

2. Więzy manipulatora w zadaniu obróbki krawędzi dyfuzora

Dla każdego zadania można określić tzw. uogólnioną powierzchnię z więzami pozycyjnymi na kierunkach normalnych do tej powierzchni i więzami siłowymi na kierunkach do niej stycznych [5, 13]. Pojęcie więzów pozycyjnych odnosi się do więzów narzuconych na pozycję i orientację końcówki roboczej manipulatora, natomiast pojęcie więzów siłowych odnosi się do więzów narzuconych na siły i momenty interakcji końcówki z obrabianym przedmiotem. Więzy te rozdzielają dopuszczalne ruchy końcówki manipulatora na dwa ortogonalne zbiory, a ruchy te muszą być sterowane wg odmiennych kryteriów.

Na rys. 3 określono zestaw więzów naturalnych i sztucznych, pozycyjnych oraz siłowych dla przypadku obróbki krawędzi dyfuzora za pomocą pilnika zamocowanego w końcówce manipulatora w przypadku dokładnie znanej geometrii krawędzi *k*.

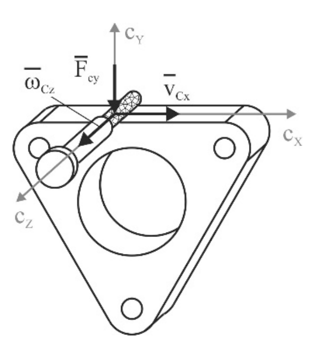

więzy naturalne	
pozycyjne	siłowe
$v_{Cy} = 0$ $\omega_{Cx} = 0$	$F_{Cx} = 0$ $F_{Cz} = 0$ $M_{Cy} = 0$ $M_{Cz} = 0$
więzy sztuczne	
pozycyjne	siłowe
$v_{Cx} = \alpha_1$ $v_{Cz} = 0$ $\omega_{Cy} = 0$ $\omega_{Cz} = \alpha_2$	$F_{Cy} = \alpha_3$ $M_{Cx} = 0$

Rys. 3. Więzy naturalne i sztuczne w zadaniu obróbki krawędzi dyfuzora silnika

Fig. 3. Natural and artificial constraints in the task of machining of the engine diffuser edge

Zadanie określono względem układu więzów $\{c\}$, który jest związany z uchwytem narzędzia i porusza się wraz z nim. Obok rysunku podano więzy naturalne dla rozważanego zadania. Zostanie teraz wyjaśniony sens tych więzów. Ruch narzędzia przez powierzchnię nie jest możliwy czyli ograniczona jest translacja wzdłuż osi c_Y oraz rotacja względem osi c_X, dlatego v_{Cy}=0 i ω_{Cx}=0. Więzy pozycyjne określono tu przez podanie wartości prędkości. W przypadku pominięcia oporów ruchu występujących pomiędzy pilnikiem i powierzchnią dyfuzora okazuje się, że nie jest możliwe wywarcie siły na kierunkach osi $\mathrm{c_X}$ i $\mathrm{c_Z}$ oraz momentu względem osi c_Y i c_Z, dlatego F_{Cx}=0, F_{Cz}=0, M_{Cy}=0 i M_{Cz}=0. Jest to uproszczenie przyjęte w celu uczynienia opisu procesu obróbki bardziej przejrzystym.

Uzupełnieniem więzów naturalnych są więzy sztuczne, które powstają przez podanie żądanego ruchu końcówki lub żądanej siły wywieranej przez nią. Tak jak więzy naturalne, również więzy sztuczne określa się na kierunkach normalnych i stycznych do uogólnionej powierzchni z tą różnicą, że na kierunkach normalnych do uogólnionej powierzchni są określane sztuczne więzy siłowe, zaś na kierunkach stycznych są określane sztuczne więzy pozycyjne. Nie ma więc sprzeczności pomiędzy więzami naturalnymi i sztucznymi.

W czasie obróbki krawędzi końcówka musi wykonywać ruch postępowy z prędkością α_1 względem osi c_X, dlatego $v_{Cx}=\alpha_1$, natomiast ruch postępowy względem osi c_Z jest niedopuszczalny, gdyż narzędzie nie powinno tracić kontaktu z obrabianą powierzchnią, dlatego $v_{Cz}=0$. Obrót narzędzia względem osi c_Y nie jest konieczny, dlatego $\omega_{Cy}=0$. Aby obróbka była możliwa narzędzie musi wykonywać obrót względem osi c_Z z prędkością kątową α_2 i być dociskane do powierzchni z odpowiednią siłą α_3 na kierunku c_Y, stąd $\omega_{Cz}=\alpha_2$ oraz $F_{Cy}=\alpha_3$. Wywieranie momentu względem osi c_X nie jest korzystne w rozpatrywanym procesie, dlatego $M_{Cx}=0$.

W celu zaplanowania ruchu końcówki roboczej manipulatora (przyjęto, że będzie to arbitralnie wybrany punkt D) należy podać matematyczny opis kształtu obrabianej krawędzi. Będzie to równanie więzów narzuconych na ruch końcówki manipulatora. Ze względu na kształt krawędzi podzielono ją na sześć części (rys. 4), z których każda będzie opisana odrębnymi równaniami.

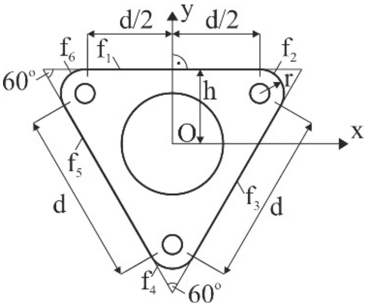

Rys. 4. Geometria dyfuzora

Fig. 4. Geometry of the diffuser

$$\begin{cases} f_1 = y_D - h = 0, \\ x_D \in \left\langle -\dfrac{d}{2}, \dfrac{d}{2} \right\rangle \end{cases} \tag{1}$$

$$\begin{cases} f_2 = \left(x_D - \dfrac{d}{2} \right)^2 + \left(y_D - h + r \right)^2 - r^2 = 0, \\ y_D \in \left\langle h, h - \dfrac{3}{2} r \right\rangle \end{cases} \tag{2}$$

$$\begin{cases} f_3 = y_D - \sqrt{3}x_D + 2h = 0, \\ y_D \in \left\langle h - \frac{3}{2}r, h - \frac{3}{2}r - \frac{\sqrt{3}}{2}d \right\rangle \end{cases} \tag{3}$$

$$\begin{cases} f_4 = x_D^2 + \left(y_D + 2h - 2r\right)^2 - r^2 = 0, \\ x_D \in \left\langle \frac{\sqrt{3}}{2}r, -\frac{\sqrt{3}}{2}r \right\rangle \end{cases} \tag{4}$$

$$\begin{cases} f_5 = y_D + \sqrt{3}x_D + 2h = 0, \\ y_D \in \left\langle h - \frac{3}{2}r - \frac{\sqrt{3}}{2}d, h - \frac{3}{2}r \right\rangle \end{cases} \tag{5}$$

$$\begin{cases} f_6 = \left(x_D + \frac{d}{2}\right)^2 + \left(y_D - h + r\right)^2 - r^2 = 0, \\ y_D \in \left\langle h - \frac{3}{2}r, h \right\rangle \end{cases} \tag{6}$$

gdzie: $f_1, \ldots, f_6$ – równania więzów (krawędzi dyfuzora),
d, h, r – wielkości geometryczne charakteryzujące dyfuzor (rys. 3),
x_D, y_D – współrzędne punktu D – końcówki manipulatora.

Równania (1) – (6) to równania więzów geometrycznych skleronomicznych dwustronnych [1, 14] narzuconych na ruch końcówki roboczej manipulatora. Zależności (1), (3) i (5) to równania prostych, natomiast zależności (2), (4) i (6) to równania okręgów. Z powyższych wzorów wynika, że równania więzów będą się zmieniać przedziałami podczas ruchu końcówki manipulatora.

3. Trajektoria pozycyjna i siłowa

Do określenia trajektorii pozycyjnej końcówki roboczej (punktu D) zastosowane zostaną równania (1) – (6) interpretowane jako równania toru końcówki. Wektor prędkości punktu D w płaszczyźnie xy to

$$\mathbf{v}_D = \begin{bmatrix} \dot{x}_D \\ \dot{y}_D \end{bmatrix} \tag{7}$$

gdzie: $\mathbf{v}_D$ – wektor prędkości punktu D,

$\dot{x}_D$, $\dot{y}_D$ – składowe prędkości punktu D.

Wartość prędkości określa wzór

$$v_D = \sqrt{\dot{x}_D^2 + \dot{y}_D^2} \tag{8}$$

gdzie: v_D – wartość prędkości punktu D.

Wektor prędkości musi być styczny do toru aby prędkość punktu D była możliwa do zrealizowania, muszą więc być spełnione następujące równania

$$\begin{cases} grad f_1 \cdot \mathbf{v}_D = 0, \\ grad f_2 \cdot \mathbf{v}_D = 0, \\ \vdots \\ grad f_6 \cdot \mathbf{v}_D = 0 \end{cases} \tag{9}$$

które po rozwinięciu będą miały postać

$$\begin{cases} f_{1x}\dot{x}_D + f_{1y}\dot{y}_D = 0, \\ f_{2x}\dot{x}_D + f_{2y}\dot{y}_D = 0, \\ \vdots \\ f_{6x}\dot{x}_D + f_{6y}\dot{y}_D = 0 \end{cases} \tag{10}$$

gdzie: $f_{ix} = \dfrac{\partial f_i}{\partial x_D}$, $f_{iy} = \dfrac{\partial f_i}{\partial y_D}$, i=1,2,…,6.

Rozwiązując równania (8) i (10) dla każdego z sześciu fragmentów toru otrzymano równania określające składowe prędkości punktu D w następującej formie

$$\begin{cases} \dot{x}_D = \mp \dfrac{f_{iy} v_D}{\sqrt{f_{ix}^2 + f_{iy}^2}}, \\ \dot{y}_D = \pm \dfrac{f_{ix} v_D}{\sqrt{f_{ix}^2 + f_{iy}^2}} \end{cases} \tag{11}$$

W analizowanym przypadku będzie

$$\begin{cases} f_{1x} = 0,\ f_{1y} = 1, \\ f_{2x} = 2\left(x_D - \dfrac{d}{2}\right),\ f_{2y} = 2\left(y_D - h + r\right), \\ f_{3x} = -\sqrt{3},\ f_{3y} = 1, \\ f_{4x} = 2x_D,\ f_{4y} = 2\left(y_D + 2h - 2r\right), \\ f_{5x} = \sqrt{3},\ f_{5y} = 1, \\ f_{6x} = 2\left(x_D + \dfrac{d}{2}\right),\ f_{6y} = 2\left(y_D - h + r\right) \end{cases} \tag{12}$$

Układ (11) to układ równań różniczkowych, które po rozwiązaniu z warunkami początkowymi wynikającymi z przyjętego toru ruchu punktu D (rys. 5a), posłużą do wygenerowania przebiegów czasowych przemieszczeń i składowych prędkości końcówki manipulatora w płaszczyźnie *xy*. Podczas rozwiązywania układu równań (11) należy uwzględnić sześć przedziałów. Wartość prędkości punktu D wynika z przyjętych sztucznych więzów pozycyjnych określonych w rozdziale 2, czyli $v_D = v_{Cx} = \alpha_1$. Prędkość ruchu końcówki manipulatora wynika z założeń dotyczących realizacji procesu technologicznego. Przyjmuje się profil prędkości zawierający fazę rozpędzania, ruchu ze stałą prędkością oraz fazę hamowania, który często jest profilem trapezowym. W celu zapewnienia istnienia ciągłych pochodnych funkcji prędkości, profil trapezowy aproksymowano funkcją uwzględniającą okresy przejściowe pomiędzy poszczególnymi fazami ruchu (rys. 5b), czyli

$$v_D = \frac{v_{D\max}}{1 + \exp\left[-c_P\left(t - t_1\right)\right]} - \frac{v_{D\max}}{1 + \exp\left[-c_P\left(t - t_2\right)\right]} \tag{13}$$

gdzie: $v_{D\max} = 0.01$ m/s - wartość maksymalna prędkości,

$c_P = 10$ 1/s - współczynnik wpływający na długość fazy rozpędzania i hamowania (zwiększenie jego wartości powoduje skrócenie tych faz),

$t_1 = 5$ s - czas, w którym $v_D = v_{D\max}/2$ podczas fazy rozpędzania,

$t_2 = 33$ s - czas, w którym $v_D = v_{D\max}/2$ podczas hamowania,

$t \in \langle 0, 40 \rangle$ s.

W wyniku numerycznego rozwiązania równań (11) uzyskano trajektorię pozycyjną przedstawioną na rys. 6.

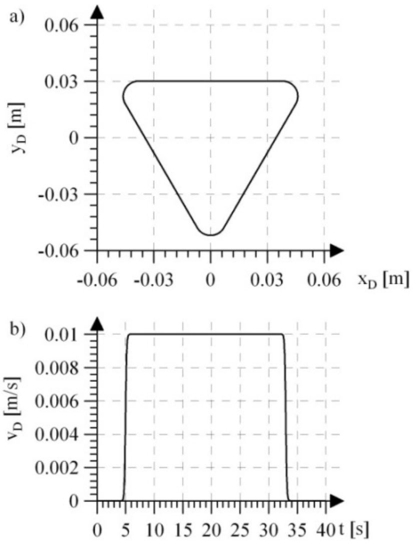

Rys. 5. a) tor ruchu, b) profil prędkości końcówki roboczej manipulatora

Fig. 5. a) path of motion, b) the velocity profile of the end effector of manipulator

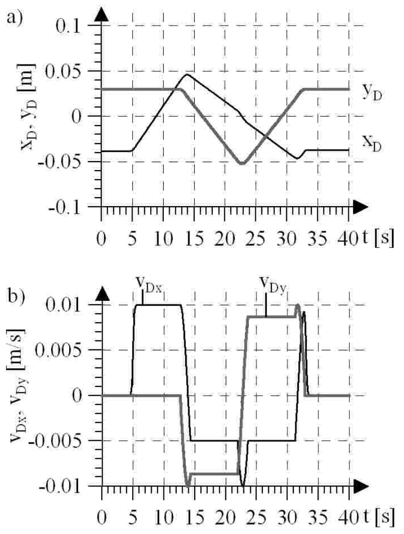

Rys. 6. Trajektoria pozycyjna: a) przemieszczenia końcówki roboczej, b) składowe prędkości końcówki

Fig. 6. Positional trajectory: a) displacements of the end effector, b) components of velocity

Wartość prędkości kątowej narzędzia $\omega=\omega_{Cz}=\alpha_2$ przyjęto następująco (rys. 7):

$$\omega=\frac{\omega_{\max}}{1+\exp\left[-c_P\left(t-t_1\right)\right]}-\frac{\omega_{\max}}{1+\exp\left[-c_P\left(t-t_2\right)\right]} \tag{14}$$

gdzie: $\omega_{\max}$=1500 rad/s - wartość prędkości kątowej narzędzia,
c_P=10 1/s - współczynnik wpływający na długość fazy rozpędzania i hamowania,
t_1=3 s - czas, w którym $\omega=\omega_{\max}/2$ podczas fazy rozpędzania narzędzia,
t_2=35 s - czas, w którym $\omega=\omega_{\max}/2$ podczas hamowania narzędzia,
$t\in\left\langle 0,40\right\rangle$ s.

Wartość siły docisku narzędzia do obrabianej powierzchni wynika z przyjętych sztucznych więzów siłowych, czyli

$$F=F_{Cy}=\alpha_3 \tag{15}$$

Stanowi to trajektorię siłową przyjętą w postaci następującego równania (rys. 8)

$$F = \frac{F_{\max}}{1+\exp\left[-c_F\left(t-t_1\right)\right]} - \frac{F_{\max}}{1+\exp\left[-c_F\left(t-t_2\right)\right]} \tag{16}$$

gdzie: $F_{\max}$=10 N – wartość siły docisku,
t_1=5 s - czas, w którym F=$F_{\max}$/2 podczas fazy zwiększania docisku,
t_2=33 s - czas, w którym F=$F_{\max}$/2 podczas zmniejszania docisku,
c_F=10 1/s.

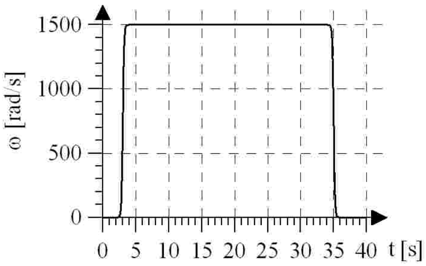

Rys. 7. Prędkość kątowa narzędzia

Fig. 7. The angular velocity of the tool

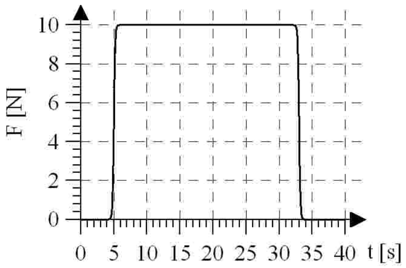

Rys. 8. Trajektoria siłowa

Fig. 8. Force trajectory

4. Więzy manipulatora w zadaniu wiercenia otworu

W przypadku zadania wiercenia otworu zestaw więzów będzie taki jak na rys. 9. Zadanie określono względem układu więzów $\{c\}$ związanego z narzędziem i poruszającego się wraz z nim. W przypadku operacji wiertarskiej można zadać prędkość obrotową wiertła $\omega_{Cz}=\alpha_4$ i prędkość jego posuwu $v_{Cz}=\alpha_3$. Ruchom tym towarzyszą na tyle duże siły interakcji, że trudno przyjąć uproszczenie polegające na ich pominięciu. Dlatego na rys. 8 podano również naturalne więzy siłowe występujące podczas procesu i są to: siła interakcji $F_{Cz}=\alpha_1$ i moment interakcji $M_{Cz}=\alpha_2$ na kierunku osi c_Z. Prędkości oraz siły i momenty względem pozostałych osi powinny być zerowe, aby nie nastąpiło złamanie wiertła. Można również przyjąć inny, być może bardziej intuicyjny wariant więzów sztucznych, zadając siłę $F_{Cz}=\alpha_1$ i rozumiejąc ją jako sztuczny więz siłowy. Wówczas prędkość $v_{Cz}=\alpha_3$ będzie zaliczona do naturalnych więzów pozycyjnych i będzie funkcją siły F_{Cz} i właściwości materiału, w którym wykonywana jest operacja wiercenia. Podobnie można uczynić z parą więzów $M_{Cz}=\alpha_2$ i $\omega_{Cz}=\alpha_4$. Reasumując, można narzucić więzy pozycyjne, a siły interakcji nie będą sterowane, lub sterować siłami interakcji, a kinematyczne parametry procesu wiercenia będą ich funkcją.

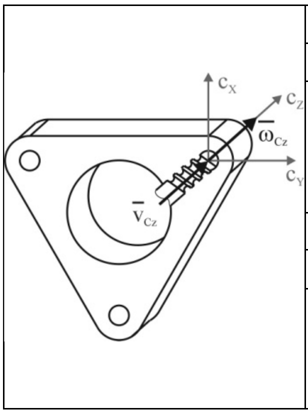

więzy naturalne	
pozycyjne	siłowe
$v_{Cx} = 0$ $v_{Cy} = 0$ $\omega_{Cx} = 0$ $\omega_{Cy} = 0$	$F_{Cz} = \alpha_1$ $M_{Cz} = \alpha_2$
więzy sztuczne	
pozycyjne	siłowe
$v_{Cz} = \alpha_3$ $\omega_{Cz} = \alpha_4$	$F_{Cx} = 0$ $F_{Cy} = 0$ $M_{Cx} = 0$ $M_{Cy} = 0$

Rys. 9. Więzy naturalne i sztuczne w zadaniu wiercenia otworu

Fig. 9. Natural and artificial constraints in the task of hole drilling

Przyjmując pierwszy wariant więzów, podany na rys. 9, zadano przebiegi prędkości liniowej i kątowej wiertła. Wartość prędkości posuwu wiertła wynika z przyjętych sztucznych więzów pozycyjnych, czyli v_D=v_{Cz}=α_3. Wartość prędkości v_D przyjęto wg wzoru (13), gdzie założono $v_{D\max}$=0.001 m/s (rys. 10a). Wartość prędkości kątowej wiertła ω=ω_{Cz}=α_4 przyjęto wg wzoru (14), gdzie założono $\omega_{\max}$=50 rad/s (rys. 10b).

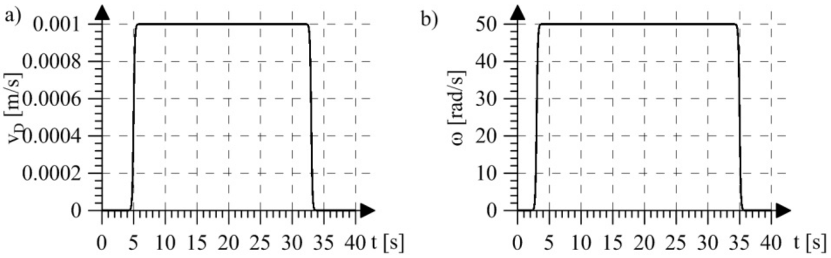

Rys. 10. Trajektoria pozycyjna końcówki roboczej w procesie wiercenia: a) prędkość posuwu wiertła, b) prędkość kątowa wiertła

Fig. 10. The positional trajectory of the end effector in the drilling process: a) the feed rate of the drill, b) the angular velocity of the drill

5. Podsumowanie

W wyniku analizy więzów końcówki roboczej manipulatora wynikających z założonego do realizacji zadania uzyskano trajektorię jej ruchu w przestrzeni roboczej. Tak zaplanowana trajektoria stanowi trajektorię zadaną układu sterowania i musi zostać zrealizowana w celu wykonania zadania. Realizacja wymienionych strategii obróbki krawędzi dyfuzora i wpływ wybranej strategii na jakość obróbki będą przedmiotem dalszych prac badawczych.

Literatura

[1] Blajer W.: Metody dynamiki układów wieloczłonowych, Monografie 35, Politechnika Radomska, Radom 1998.

[2] Burghardt A., Kurc K., Szybicki D.: Projekt zrobotyzowanego stanowiska z kontrolą siły, XIV Konf. Automatyzacji i Eksploatacji Systemów Sterowania i Łączności, ASMOR 2013, Jastrzębia Góra 2013.

[3] Burghardt A., Muszyńska M., Jagiełowicz-Ryznar C., Żylski W.: Aplikacja systemu wizyjnego do automatycznej adaptacji trajektorii narzędzia, XIV Konf. Automatyzacji i Eksploatacji Systemów Sterowania i Łączności, ASMOR 2013, Jastrzębia Góra 2013.

[4] Canudas de Wit C., Siciliano B., Bastin G.: Theory of Robot Control, Springer, London 1996.

[5] Craig J.J.: Wprowadzenie do robotyki, WNT, Warszawa 1995.

[6] Gierlak P.: Hybrid position/force control in robotised machining, Solid State Phenomena, 210 (2014) 192-199.

[7] Gierlak P.: Hybrid position/force control of the SCORBOT-ER 4pc manipulator with neural compensation of nonlinearities, in: L. Rutkowski et al. (eds.): ICAISC 2012, Part II, LNCS 7268, pp. 433-441, Springer-Verlag, Berlin, Heidelberg 2012.

[8] Gierlak P.: Model matematyczny kartezjańskiego manipulatora własnej konstrukcji, ZN PRz, Mechanika, 88 (2016) 115-125.

[9] Gierlak P.: Zastosowanie adaptacyjnego hybrydowego pozycyjno-siłowego sterowania manipulatorem w zrobotyzowanej obróbce mechanicznej, Modelowanie Inżynierskie, 15 (2013) 28-34.

[10] Gierlak P., Muszyńska M.: Inteligentne sterowanie ruchem robota manipulacyjnego z więzami geometrycznymi, Modelowanie Inżynierskie, 19 (2014) 19-24.

[11] Hendzel Z., Burghardt A., Gierlak P., Szuster M.: Conventional and fuzzy force control in robotised machining, Solid State Phenomena, 210 (2014) 178-185.

[12] Sabanović A, Ohnishi K.: Motion control systems, John Willey & Sons (Asia) Pte Ltd., Singapore 2011.

[13] Spong M.W., Vidyasagar M.: Dynamika i sterowanie robotów, WNT, Warszawa 1997.

[14] Susłow G. K.: Mechanika teoretyczna, PWN, Warszawa 1960.

[15] Winiarski T., Zieliński C.: Podstawy sterowania siłowego w robotach, PAR, 12 (2008) 5-10.

[16] Yu F., Minami M., Maeba T., Yanou A.: Constraint-combined force/position hybrid control method with Lyapunov stability, Proc. SICE Annual Conference, 2011, pp. 671-676.

[17] http://www.ati-ia.com

[18] http://www.fanucrobotics.pl

[19] http://www.rad-ra.com

[20] http://www.schunk.com

THE MANIPULATOR CONSTRAINTS ANALYSIS IN THE TASK OF ROBOTISED MACHINING OF DIFFUSER

Summary

This paper presents the analysis of the geometrical constraints of the robotic manipulator end effector, the task of which is the realisation of the diffuser machining. In terms of control theory, the realisation of this task is considered as a control of an object with partial movement restrictions. It requires determination of the desired trajectory of the robot's control system understood as so-called *position and force* trajectory. In this paper the geometry of the diffuser and the mathematical description of edges that will be deburred, are presented. The sets of natural and artificial, position and force constraints for this task and for task of hole drilling are given. The procedure of determining position and force trajectory which will be the reference trajectory of robot's control system is provided. The simulation results of generating robot's tip trajectory are presented.

Keywords: geometrical constraints, robotic manipulator, trajectory planning, robotized machining

DOI: 10.7862/rm.2016.16

Otrzymano/received: 14.09.2016 r.
Zaakceptowano/accepted: 28.09.2016 r.

ZESZYTY NAUKOWE POLITECHNIKI RZESZOWSKIEJ 293, Mechanika 88
RUTMech, t. XXXIII, z. 88 (3/16), lipiec-wrzesień 2016, s. 213-220

Alexander SCHREK[1]
Pavol ŠVEC[2]
Veronika GAJDOŠOVÁ[3]

DEEP DRAWING OF TAILOR-WELDED BLANKS MADE OF HIGH-STRENGTH STEEL

A comparison study was conducted to evaluate the deep drawing of a rectangular box from tailor-welded blank, composed of two parts of different thicknesses. The blank material is high strength steel with transformation induced plasticity, and the weld line is located in the blank centre at the beginning of the deep drawing. The study is focused on the weld line movement during the deep drawing with quasi uniform or controlled non-uniform distribution of the blankholder pressure, which is applied on the flange of the blank. The goal is to minimise the weld line movement and to improve the formability of the tailor-welded blank.

Keywords: deep drawing, tailor-welded blank, simulation, weld line

1. Introduction

Tailored blanks for deep-drawing, consisting of parts of the same type of material but of a different thickness or of different grades of material are now widely used in the automotive industry for car body and other structures. The main advantages of their use are a reduction of the tools number, decreasing assembly costs, material savings, avoiding spot welding, weight reduction, improved accuracy and structural integrity, etc. On the other hand, as disadvantages can be mentioned additional costs for technology design, often reduced formability of parts material, uneven plastic flow during drawing and instability of weld line position [1-3].

There are several types of tailored blanks. The major part includes tailor-welded blanks (TWB) prepared by laser welding of particular parts. Specialised manufacturers offer tailor-rolled blanks (TRB) with non-constant thickness for large purchasers. A comparison of both types of preparation sounds

---

[1] Autor do korespondencji/corresponding author: Alexander Schrek, Slovak University of Technology, Námestie slobody 17, 812 31 Bratislava, Slovakia, e-mail: alexander.schrek@stuba.sk

[2] Pavol Švec, Slovak University of Technology, e-mail: pavol.svec@stuba.sk

[3] Veronika Gajdošová, Slovak University of Technology, e-mail: veronika.gajdosova@stuba.sk

generally in favor of the rolling. Such a production is cheaper only for a high-volume production. The thickness change can be oriented only in the direction perpendicular to the rolling direction and it is not possible to achieve a significanlty different stress-strain properties of the blank [1].

High-strength transformation induced plasticity (TRIP) steels, often used for TWBs belong to the steel grades, whose application is possible to obtain desired properties of the drawn parts for car body structure. It has also a positive impact on the weight reduction of components, in some cases up to 20% with subsequent reduction of fuel consumption. Increased rigidity, strength of the support structure and the ability to absorb energy during a car accident positively influence the safety of cars. The usage of these high-strength steels increases deformation ability in a wide range of temperatures and strain rates. These properties make them suitable for the use in deformation zones, respectively as reinforcements in various parts of cars [4, 5].

One of the basic objectives of the research that is being done at the Faculty of Mechanical Engineering of Slovak University of Technology in Bratislava, is to determine the ductile properties of selected high-strength steels and TWBs, composed of these steels, and to determine the conditions for successful drawing using a tool with relatively simple customised blankholder. The paper presents some results obtained experimentally as well as using a computer simulation when drawing of rectangular boxes from the TRIP 780 TWBs [6].

2. Experimental procedure

A forming tool with blankholder for simple drawing of rectangular box was designed and manufactured. The punch was anchored to a bottom bolster connected to the lower base of the PYE 160 press operated with a nominal force 160 kN. Transmission pillars, which pass through the bottom bolster, transmit the power to the blankholder created by lower base of the press. The die is located on the upper arm . The drawn part is formed when moving die in relation to static punch. The arm of the press creates the tensile force and combined with the base it creates the blankholder force. The blankholder plate is quasi-elastic and able to transmit uneven pressure on the flange of blank. The pressure is created by transmission pillars with different, adjustable height. The tool has been equipped with the force sensors. There are sensors of local forces transmitted by each pillar at four points of blankholder and sensor of total forming force transmitted by the punch. Figure 1 shows the example of the forming force variation of both the punch and the blankholder forces of particular pillars in the case of non-uniform distribution of the blankholder pressure. The forces variation is based on the height of the product [7, 8]. Figure 2 shows rectangular box created by deep drawing with dimensions of 120 mm x 80 mm and a height of approximately 40 mm. TWBs were welded from two sheets with thicknesses of 1 mm and 1.2 mm. The weld line was oriented lengthwise, crosswise or diagonally with respect to the larger dimension of the blank. Figure 3 shows the case of the crosswise position.

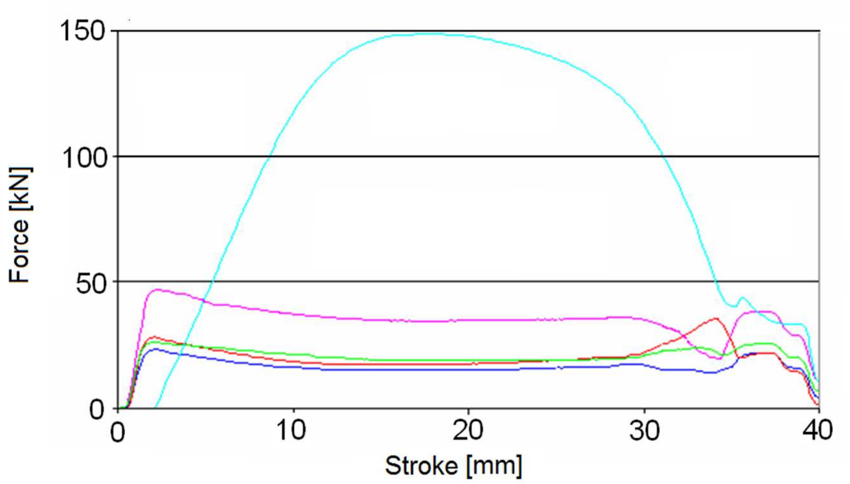

Fig.1 Variation of the forming and blankholder forces during deep drawing with non-uniform distribution of blankholder pressure, mode B: purple line– force on the pillar no. 1, blue line– force on the pillar no. 2, green line – force on the pillar no. 3, red line – force on the pillar no. 4, azure line – punch force

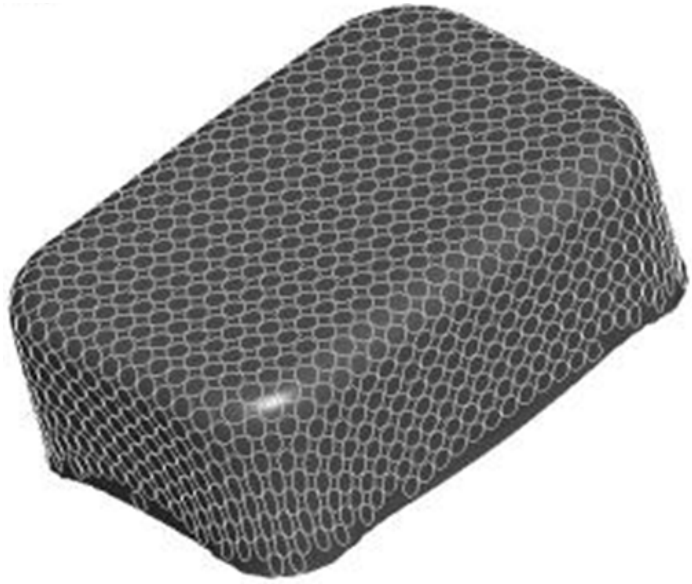

Fig. 2. Drawn part with deformation grid

Fig. 3. Bottom of the rectangular box with crosswise oriented weld line

Strain distribution on the surface of the drawn part was evaluated by an optical system based on the deformed grid. All experiments were simultaneously simulated in Dynaform software, using the experimentally determined stress-strain properties. Figure 4 shows the examples of the strain distribution when applying non-uniform pressure on the blank of constant thickness (Fig. 4a) as well as when applying uniform pressure on the TRIP 780 steel blank of non-constant thickness (Fig. 4b). The strain is determined based on the deformation of the grid, that consists of 35 elements with a diameter of 4.75 mm located along a line through the centre of the blank, upright on the weld line.

Experimentally determined behaviour of strains φ_1 and φ_2 at a blank of constant thickness and when there is non-uniform blankholder pressure with a maximum difference of 10% (Fig. 4) clearly shows differences in the bottom of created boxes in their symmetrical parts. The material flow in the right part of the bottom with higher blankholder pressure is held back against the left side. The left side of the bottom had a relatively large strain before the transition into the wall of the product. The nature of the strain distribution in the bottom is confirmed by the simulation. Asymmetry of the deformation caused by non-uniform acting of blankholder pressure is more significant when compared to the deformation φ_1 in the walls. Strain on the right side is more intensive and braking zones have also a different character. A difference of behaviour of the deformation φ_2 in right and left wall was confirmed by the simulation. When drawing TWBs with different thicknesses and quasi-uniform pressure distribution, the weld line on the bottom generally moves towards thicker material – to the left. The result is an increased plastic flow from the flange of thinner blank part into the die (right side of the figure 4b) [9].

Figure 5 shows experimentally observed and simulated distribution of major and minor strains on the rectangular boxes from TWBs. Two examples of strain distribution for two different blankholder pressure values are mentioned.

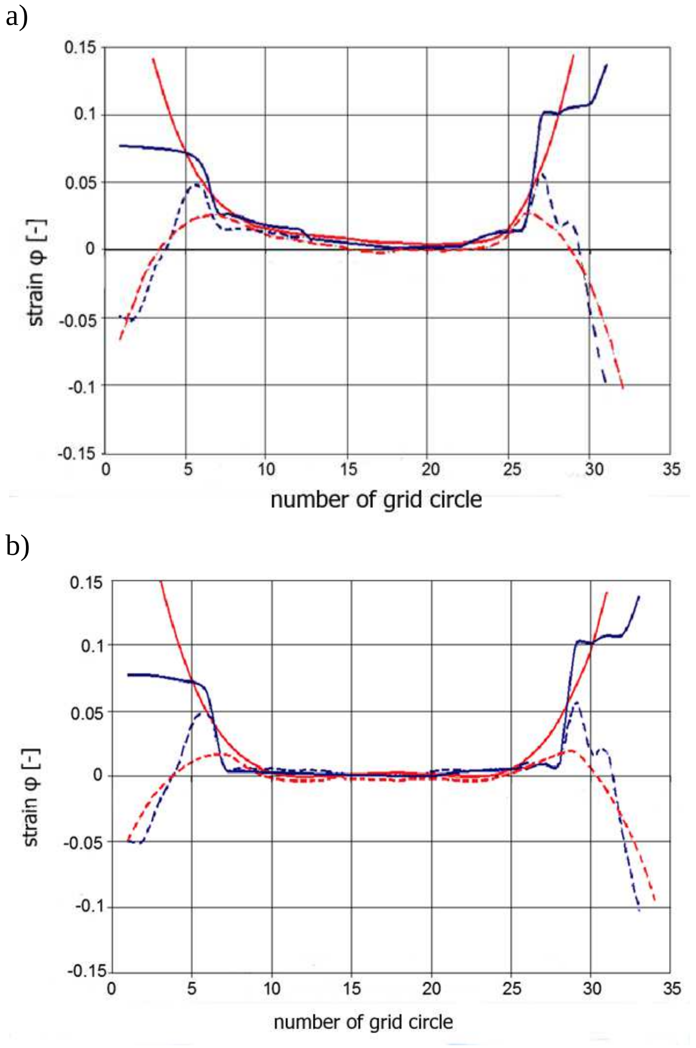

Fig. 4. The strain distribution on the part drawn from TRIP 780 steel vs. number of the elements along the middle line of the deformation grid from left to the right: a – blank with uniform thickness of 1 mm after deep drawing with non-uniform distribution of blankholder pressure, b – TWB with 1 and 1.2 mm thicknesses with uniform distribution of blankholder pressure; red line - simulation, blue line– experiment, continuous line - major strain φ_1 along the line in the middle of the box length, dashed line – minor strain φ_2 along the line in the middle of the box length

The maximum non-uniform pressure difference is 10% for A regime, and 20% for B regime. Redistribution of blankholder pressure when drawing TWB with a maximum increase of 10% on the side of the thinner blank part means a creation of conditions for a relatively uniform plastic flow with virtually no strain of the bottom of the drawn part (Fig. 5a). The strain values in the lower parts of the walls are comparable on the left and right side. An intensive increase in the wall thinning is observed on the upper part of the wall on the right side. The distribution of strain φ_2, determined experimentally and numerically, is almost symmetrical on both sides. An increase in the difference between maximum and minimum blankholder pressure to 20% (Fig. 5b) improves the drawn part symmetry. It is confirmed mainly by the simulation of strain distribution. The increase of differences of blankholder pressure causes a greater braking of material flow in the flange and increase of the strain on the part bottom.

Movement and deformation of the weld line were also a subject of the presented research. The clear result of increasing blankholder pressure on the side of the thinner material is braking the movement of the weld interface. The best result was achieved in the case of 20% difference in the pressure size. The weld line movement is also a function of its length and the initial placement on the blank [9].

3. Conclusions

TWBs made of TRIP 780 steel can be successfully drawn while producing geometrically complex products, despite their reduced formability when compared to simple blanks made of mild steel. Controlled non-uniform distribution of the blankholder pressure with quasi-elastic blankholder plate is an effective way to improve the strain distribution on the bottom and walls of the rectangular box and for braking the weld line movement. Correct adjustment of the height of the pillars transmitted the pressure on a blankholder plate allows to create the conditions for the uniform height of the box walls and small strain variations in corresponding parts of the symmetrical product.

Explicit finite element software Dynaform allows reliable simulation of drawing a blank of high-strength steel in the particular circumstances, including the strain distribution in an non-uniform and changing contact conditions in the area of blankholder. The appropriate choice of loaded system model also enables the simulation of the weld line movement, including its deformation and rotation.

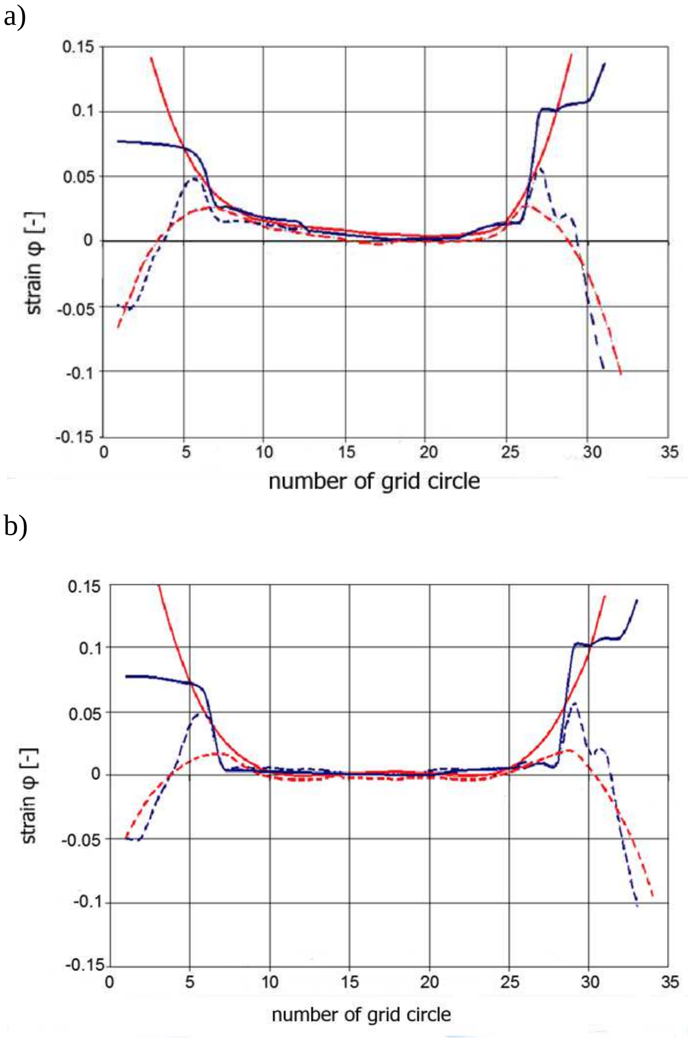

Fig. 5. The strain distribution on the part drawn from TRIP 780 steel vs. number of the elements along the middle line of the deformation grid from left to the right: a – TWB with 1 and 1.2 mm thicknesses with non-uniform distribution of blankholder pressure (mode A), b – TWB with 1 and 1.2 mm thicknesses with non-uniform distribution of blankholder pressure (mode B); red line - simulation, blue line – experiment, continuous line – major strain φ_1 along the line in the middle of the box length, dashed line – minor strain φ_2 along the line in the middle of the box length,

Acknowledgement

This work was supported by the Slovak Research and Development Agency under the contract no. APVV-0281-12

References

[1] Kinsey L.B., Wu X.: Tailor-welded blanks for advanced manufacturing, Woodhead, Cambridge 2011.

[2] Evin E., Tomáš M.: Comparison of deformation properties of steel sheets for car body parts, Procedia Eng., 48 (2012) 115-122.

[3] Frącz W., Stachowicz F., Trzepieciński T., Pieja T.: Forming limit of the heat resistant AMS 5599 sheet metal, Hutnik, 81 (2014) 442-445 (in Polish).

[4] Kestens L., Petrov R., Hubert Y.: Orientation selective transformation during intercritical annealing of cold rolled TRIP steel, Int. Conf. TRIP-Aided High Strength Ferrous Alloys, Ghent 2002, pp. 215-220.

[5] Slota J., Jurčišin M., Spišák E.: Experimental and numerical analysis of local mechanical properties of drawn part, Key Eng. Mat., 586 (2014) 245-248.

[6] Kostka P., Žitňanský P., Čekan P., Schrek A.: Numerical simulation of deep drawing of dual-phase steel, Forming the Future Innovations in Sheet Metal Forming, IDDRG 2007 Conf, Proc., Györ 2007, pp. 55-58.

[7] Schrek A., Činák M., Žitňanský P.: Experimental laboratory tooling for deep drawing process, Faculty of Mechanical Engineering, STU Bratislava. Sci. Proc. 2011, pp. 23-28.

[8] Choi Y., et al.: Investigation of welde line movements for the deep drawing process of tailored welded blanks, J. Mater. Proc. Technol. 108 (2000) 1-7.

[9] Žitňanský P., Kostka P., Schrek A.: Simulation of high strength steel deep drawing using tailored blanks, Zborník vedeckých prác Strojníckej fakulty STU, Bratislava 2010.

GŁĘBOKIE TŁOCZENIE SPAWANYCH BLACH WYKONANYCH ZE STALI WYSOKOWYTRZYMAŁEJ

Streszczenie

W artykule przedstawiono badania porównawcze oceny głębokiego tłoczenia prostokątnej wytłoczki, składającej się z dwóch części o różnej grubości, wykonanej z blachy przeznaczonej do spawania. Wsad jest wykonany z blachy wysokowytrzymałej umacnianej przez przemianę fazową, a linia spawania znajduje się w środku wsadu, w momencie rozpoczęcia procesu głębokiego tłoczenia. Badania koncentrują się na analizie przemieszczenia linii spawania w warunkach quasi- równomiernego i nierównomiernego rozkładu ciśnienia dociskacza, które jest przyłożone do kołnierza półwyrobu. Celem badań jest minimalizacja przemieszczenia linia spawania oraz poprawa odkształcalności blachy przeznaczonej do spawania.

Słowa kluczowe: głębokie tłoczenie, blacha przeznaczona do spawania, symulacja, linia spawania

DOI: 10.7862/rm.2016.17

Otrzymano/received: 31.05.2016 r.
Zaakceptowano/accepted: 14.09.2016 r.

ZESZYTY NAUKOWE POLITECHNIKI RZESZOWSKIEJ 293, Mechanika 88
RUTMech, t. XXXIII, z. 88 (3/16), lipiec-wrzesień 2016, s. 221-232

Gennady SHUSHKEVICH[1]

PROPAGATION OF THE SOUND WAVE BY AN UNCLOSED SPHERICAL SHELL AND A PENETRABLE ELLIPSOID

In this paper the result of solution of axisymmetric problem of propagation of sound wave by an unclosed spherical shell and a penetrable ellipsoid of rotation is presented. A spherical radiator is located in a thin unclosed spherical shell as a source of acoustic field. The equation of the spheroidal boundary is given in spherical coordinates. A scattered pressure field is expressed in terms of spherical wave functions. Using corresponding additional theorems the solution of boundary value problem is reduced to solving of dual equations in Legendre's polynomials, which are converted to infinite system of linear algebraic equations of the second kind. The formula for calculation of the far field and numerical results for different values of parameters are obtained.

Keywords: sound field, spherical shell, ellipsoid of rotation, dual equations, spherical radiator

1. Introduction

The study of sound waves propagation in different media has a number of practical applications in electroacoustics, hydroacoustics, medical diagnostics, bioacoustics, creation of multi-layer sound-absorbing panels against noise and vibration [1-4]. Numerous publications describe the problems of propagation of sound field by different objects and they use different analytical and numerical techniques. We will consider just a few publications related to the research topic. The propagation of the sound field by hard or soft, prolate or oblate spheroids using different techniques is considered in [5-12]. The results of the sound field propagation on permeable and elastic spheroids are studied in [13-17]. The analytical description of the acoustic field scattered by a inhomogeneous elastic spheroid is obtained in [18]. The analytical solution to the diffraction problem of the plane sound wave on an elastic spheroid with arbitrary located spherical cavity is constructed in [19].

---

[1] Autor do korespondencji/corresponding author: Gennady Shushkevich, Yanka Kupala State Universy of Grodno, 22 Ozheshko St., 230023 Grodno, Belarus, e-mail: g_shu@tut.by

In this paper analytical solution to axisymmetric problem of propagation of the sound wave by an unclosed thin spherical shell and a penetrable ellipsoid of rotation is presented. A spherical radiator is located in a thin unclosed spherical shell as a source of acoustic field. The equation of the spheroidal boundary is given in spherical coordinates. The solution of boundary value problem is reduced to solving of dual equations in Legendre's polynomials which are converted to infinite system of linear algebraic equations of the second kind. Numerical results are given for various values of parameters of the problem.

2. Problem formulation

Let a homogeneous space R^3 contain a thin unclosed spherical shell Γ_1 located on a sphere Γ of radius d with the center at point O and an ellipsoid shell S (fig. 1). We denote by D_1 the area of space bounded by the sphere Γ and by D_3 the area of space bounded by the ellipsoid shell S then $D_2 = R^3 \setminus (D_1 \cup \Gamma \cup D_3 \cup S)$ holds. The distance between points O and O_1 is equal to h_1.

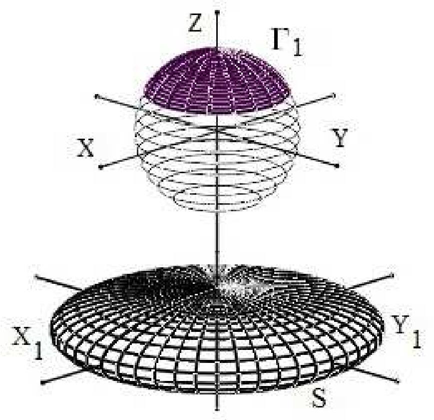

Fig. 1. Geometry of the problem

A point radiator of sound wave oscillating with an angular frequency ω is located at the point O. Areas D_j, $j=1,2,3$, are filled with material in which shear waves are not being spread. Let denote the density of medium by ρ_j and the speed of sound by c_j in D_j, $j=1,2,3$, $\rho_1=\rho_2$.

To solve this problem we introduce spherical coordinates with the point O and the point O_1. The spherical shell Γ_1 and the ellipsoid shell S are described as follows:

$$\Gamma_1 = \{r = d,\ 0 \le \theta \le \theta_0 < \pi,\ 0 \le \varphi \le 2\pi\}, \tag{1}$$

$$S = \{r_1 = r(\theta_1),\ 0 \le \theta_1 \le \pi,\ 0 \le \varphi \le 2\pi\}, \tag{2}$$

where $r(\theta_1) = a / \sqrt{1 - v\sin^2\theta_1}$, $v = e^2 / (e^2 - 1)$ stands for a prolate ellipsoid of rotation, $v = e^2$ is used for an oblate ellipsoid of rotation, e is the eccentricity of the ellipse.

Let p_c be a pressure of primary point radiator of sound field, p_j be a pressure of secondary sound field in the area D_j, $j=1,2,3$, then the real sound pressure is calculated by the formula $P_j = \mathrm{Re}\left(p_j e^{-i\omega t}\right)$.

Solution of the diffraction problem is reduced to finding pressures p_j, $j = 1, 2, 3$, which satisfy:

1) the Helmholtz equation [20]

$$\Delta p_j + k_j^2 p_j = 0 \tag{3}$$

where $\Delta = \dfrac{\partial^2}{\partial x^2} + \dfrac{\partial^2}{\partial y^2} + \dfrac{\partial^2}{\partial z^2}$ is the Laplace operator, $k_j = \omega / c_j$ is a wave number,

2) boundary condition on the surface of the spherical shell Γ_1 (acoustically hard shell):

$$\frac{\partial}{\partial \vec{n}}\left(p_c + p_1\right)\Big|_{\Gamma_1} = 0, \tag{4}$$

where $\vec{n}$ is the normal to the surface Γ_1,

3) boundary conditions on the surface of the ellipsoidal shell S:

$$p_2\big|_S = p_3\big|_S, \qquad \frac{1}{\rho_2}\frac{\partial}{\partial \vec{n}} p_2\bigg|_S = \frac{1}{\rho_3}\frac{\partial}{\partial \vec{n}} p_3\bigg|_S, \tag{5}$$

where $\vec{n}$ is the normal to the surface S and the condition at infinity [20-23]:

$$\lim_{M \to \infty} r\left(\frac{\partial p_2(M)}{\partial r} - i k p_2(M)\right) = 0, \tag{6}$$

where M is an arbitrary point at the space.

The condition of the continuity of pressure on the open part of the spherical shell $\Gamma \setminus \Gamma_1$ and the normal derivative on the surface of the sphere Γ are given by [22, 23]:

$$\left(p_c + p_1\right)\Big|_{\Gamma\setminus\Gamma_1} = p_2\Big|_{\Gamma\setminus\Gamma_1}, \qquad \frac{\partial}{\partial r}\left(p_c + p_1\right)\Big|_{\Gamma} = \frac{\partial}{\partial r} p_2\Big|_{\Gamma}. \tag{7}$$

3. Presentation of problem solution

The initial pressure of sound field can be presented in the form [21]:

$$p_c(r,\theta) = P\exp(ik_1 r)/r = P\sum_{n=0}^{\infty} f_n h_n^{(1)}\left(k_1 r\right) P_n(\cos\theta), \quad f_n = ik\delta_{0n} \tag{8}$$

where $h_n^{(1)}\left(x\right)$ are the spherical Hankel functions, $P_n(\cos\theta)$ are the Legendre polynomials, δ_{0n} is the Kronecker delta, P is constant.

The pressure of the scattered sound field presented as a superposition of the basic solutions of the Helmholtz equation in spherical coordinates taking into account the condition at infinity (6):

$$p_1(r,\theta) = P\sum_{n=0}^{\infty} a_n j_n\left(k_1 r\right) P_n\left(\cos\theta\right), \quad r < d, \tag{9}$$

$$p_2^{(1)}\left(r, \theta\right) = P\sum_{n=0}^{\infty} x_n h_n^{(1)}\left(k_1 r\right) P_n\left(\cos\theta\right), \quad r > d, \tag{10}$$

$$p_2^{(2)}\left(r_1, \theta_1\right) = P\sum_{n=0}^{\infty} y_n h_n^{(1)}\left(k_1 r_1\right) P_n\left(\cos\theta_1\right), \quad r_1 > r\left(\theta_1\right), \tag{11}$$

$$p_3(r_1,\theta_1) = P\sum_{n=0}^{\infty} b_n j_n\left(k_3 r_1\right) P_n\left(\cos\theta_1\right), \quad r_1 < r(\theta_1) \tag{12}$$

where $p_2 = p_2^{(1)}(r,\theta) + p_2^{(2)}(r_1,\theta_1)$, $j_n\left(x\right)$ are the spherical Bessel functions of the first kind.

Unknown coefficients a_n, b_n, x_n, y_n must be determined from the boundary conditions.

4. Fulfilment of boundary conditions

First, we will express function $p_2^{(2)}(r_1, \theta_1)$ through the spherical wave functions in the coordinate system with the origin at the point O using the formulae [22, 23]:

$$\left.\begin{aligned}
&h_n^{(1)}(kr_1)P_n(\cos\theta_1) = \sum_{k=0}^{\infty} A_{nk}(h_1)\, j_k(kr)P_k(\cos\theta), \quad r < h_1, \\
&A_{nk}(h_1) = (2k+1)\sum_{\sigma=|k-n|}^{k+n} i^{\sigma+k-n}\, b_\sigma^{(n0k0)}\, h_\sigma^{(1)}(kh_1), \\
&b_\sigma^{(n0q0)} = (nq00\,|\,\sigma 0)^2, \quad (nq00\,|\,\sigma 0) \text{ are the Clebsch} - \text{Gordan coefficients,}
\end{aligned}\right\} \qquad (13)$$

then

$$p_2^{(2)}(r, \theta) = P\sum_{n=0}^{\infty} p_n\, j_n(k_1 r)P_n(\cos\theta), \; p_n = \sum_{k=0}^{\infty} y_k A_{kn}(h_1) \qquad (14)$$

Considering (8)-(10), (14) and taking into account the condition of orthogonality of the Legendre polynomials on the interval $[0; \pi]$ the boundary conditions (4), (7) will become:

$$\left.\begin{aligned}
&\sum_{n=0}^{\infty} x_n \frac{d}{d\xi_0} h_n^{(1)}(\xi_0)P_n(\cos\theta) = -\sum_{n=o}^{\infty} p_n \frac{d}{d\xi_0} j_n(\xi_0)P_n(\cos\theta), \quad 0 \le \theta < \theta_0, \\
&\sum_{n=0}^{\infty} \frac{x_n - f_n}{\frac{d}{d\xi_0} j_n(\xi_0)} P_n(\cos\theta) = 0, \quad \theta_0 < \theta \le \pi, \quad \xi_0 = k_1 d.
\end{aligned}\right\} \qquad (15)$$

We introduce new coefficients X_n by the formula

$$x_n = X_n \frac{d}{d\xi_0} j_n(\xi_0) + f_n, \quad n = 0, 1, ... \qquad (16)$$

and the small parameter

$$g_n = 1 + \frac{4i\xi_0^3}{2n+1} \frac{d}{d\xi_0} j_n(\xi_0) \frac{d}{d\xi_0} h_n^{(1)}(\xi_0) \; . \qquad (17)$$

From the asymptotic representations for functions $j_n(x), h_n^{(1)}(x)$, where $n \gg x$ [21]:

$$j_n(x) \approx \frac{2^n n!(x)^n}{(2n+1)!}, \quad h_n^{(1)}(x) \approx -\frac{i(2n)!}{2^n n!(x)^n}, \tag{18}$$

follows that $g_n = O\left(n^{-2}\right)$.

The dual series equations (15) take the form

$$\left.\begin{aligned}&\sum_{n=0}^{\infty}(2n+1)(1-g_n)X_n P_n(\cos\theta) = \sum_{n=o}^{\infty}(2n+1)(\tilde{f}_n + \tilde{p}_n)P_n(\cos\theta), \; 0 \le \theta < \theta_0, \\ &\sum_{n=0}^{\infty} X_n P_n(\cos\theta) = 0, \quad \theta_0 < \theta \le \pi,\end{aligned}\right\} \tag{19}$$

where

$$\tilde{f}_n = 4i\xi_0^3 f_n \frac{d}{d\xi_0} h_n^{(1)}(\xi_0)/(2n+1), \quad \tilde{p}_n = 4i\xi_0^3 a_n \frac{d}{d\xi_0} j_n(\xi_0)/(2n+1). \tag{20}$$

The dual series equations are transformed to the infinite system of linear algebraic equations of the second kind with the completely continuous operator using the integral representation for the Legendre polynomials [22]:

$$X_n - \sum_{k=0}^{\infty} g_k R_{nk}(\theta_0) X_k = \sum_{k=0}^{\infty}\left(\tilde{p}_k + \tilde{f}_k\right) R_{nk}(\theta_0), \quad n = 0, 1, \ldots, \tag{21}$$

where

$$R_{nk}(\theta_0) = \frac{1}{\pi}\left[\frac{\sin(n-k)\theta_0}{n-k} - \frac{\sin(n+k+1)\theta_0}{n+k+1}\right], \quad \left.\frac{\sin(n-k)\theta_0}{n-k}\right|_{n=k} = \theta_0 \,. \tag{22}$$

Now we present the function $p_2^{(1)}(r, \theta)$ through the spherical wave functions in the coordinate system with origin at the point O$_1$ using formula [22, 23]:

$$h_n^{(1)}(kr) P_n(\cos\theta) = \sum_{k=0}^{\infty} B_{nk}(h_1) j_k(kr_1) P_k(\cos\theta_1), \quad r_1 < h_1, \tag{23}$$

then

$$p_2^{(1)}\left(r_1,\,\theta_1\right)=P\sum_{n=0}^{\infty}z_n j_n(k_1r_1)P_n\left(\cos\theta_1\right),\; z_n=\sum_{p=0}^{\infty}x_pB_{pn}\left(h_1\right), \tag{24}$$

where

$$B_{nk}(h_1)=\left(2k+1\right)\sum_{\sigma=|k-n|}^{k+n}(-1)^{\sigma}\,i^{\sigma+k-n}\,b_{\sigma}^{(n0k0)}\,h_{\sigma}^{(1)}(k_1h_1)\,. \tag{25}$$

In view of the fact that

$$\left.\begin{array}{l}\dfrac{\partial}{\partial\vec{n}}p_j(r_1,\theta_1)\Big|_S=\dfrac{\partial}{\partial r_1}p_j(r_1,\theta_1)-\dfrac{r'(\theta_1)}{r(\theta_1)^2}\dfrac{\partial}{\partial\theta_1}p_j(r_1,\theta_1)\Big|_{r_1=r(\theta_1)},\quad j=2,3,\\[2ex] \dfrac{d}{d\theta_1}P_n(\cos\theta_1)=P_n^1(\cos\theta_1),\end{array}\right\} \tag{26}$$

boundary conditions (5) together with (11), (12), (24) take the form

$$\left.\begin{array}{l}\displaystyle\sum_{n=0}^{\infty}z_n j_n(k_1r(\theta_1))P_n\left(\cos\theta_1\right)+\sum_{n=0}^{\infty}y_nh_n^{(1)}\left(k_1r(\theta_1)\right)P_n\left(\cos\theta_1\right)=\\[2ex] \displaystyle=\sum_{n=0}^{\infty}b_nj_n\left(k_3r(\theta_1)\right)P_n\left(\cos\theta_1\right),\end{array}\right\} \tag{27}$$

$$\left.\begin{array}{l}\displaystyle\sum_{n=0}^{\infty}z_nk_1j_n'(\xi_1)P_n(\cos\theta_1)-\frac{r'(\theta_1)}{r(\theta_1)^2}j_n(\xi_1)P_n^1(\cos\theta_1)+\\[2ex] \displaystyle+\sum_{n=0}^{\infty}y_nk_1h_n^{(1)\prime}(\xi_1)P_n(\cos\theta_1)-\frac{r'(\theta_1)}{r(\theta_1)^2}h_n^{(1)}(\xi_1)P_n^1(\cos\theta_1)\;=\\[2ex] \displaystyle=\frac{\rho_1}{\rho_3}\sum_{n=0}^{\infty}b_nk_3j_n'(\xi_3)P_n(\cos\theta_1)-\frac{r'(\theta_1)}{r(\theta_1)^2}j_n(\xi_3)P_n^1(\cos\theta_1),\;\xi_j=k_jr(\theta_1),\;j=1,3.\end{array}\right\} \tag{28}$$

Let eliminate coefficients z_n in (27), (28) using (24), (16). We multiply the resulting equations by $P_s\left(\cos\theta\right)\sin\theta d\theta$, $s=0,1,2,...$, and integrate from 0 to π, and link with (21) then we have

$$\left.\begin{aligned}
&\sum_{n=0}^{\infty}(g_n R_{sn}(\theta_0)-\delta_{ns})X_n+\sum_{n=0}^{\infty}\tilde{b}_{ns}(k_1)y_n=4\xi_0^3 k_1\frac{d}{d\xi_0}h_0^{(1)}(\xi_0)R_{s0}(\theta_0), s=0,1,2,...,\\
&\sum_{n=0}^{\infty}X_n\tilde{a}_{ns}(k_1)+\sum_{n=0}^{\infty}y_n b_{ns}(k_1)-\sum_{n=0}^{\infty}b_n a_{ns}(k_3)=-ik_1\sum_{n=0}^{\infty}B_{0n}(h_1)a_{ns}(k_1),\\
&\sum_{n=0}^{\infty}X_n\tilde{A}_{ns}(k_1)+\sum_{n=0}^{\infty}y_n B_{ns}(k_1)-\frac{\rho_3}{\rho_1}\sum_{n=0}^{\infty}b_n A_{ns}(k_3)=-ik_1\sum_{n=0}^{\infty}B_{0n}(h_1)\,A_{ns}(k_1),
\end{aligned}\right\}\qquad(29)$$

where

$$\left.\begin{aligned}
&a_{n,s}(k_j)=\int_0^{\pi}j_n(\xi_j)P_n(\cos\theta_1)P_s(\cos\theta_1)\sin\theta_1 d\theta_1.\\
&b_{n,s}(k_1)=\int_0^{\pi}h_n^{(1)}(\xi_j)P_n(\cos\theta_1)P_s(\cos\theta_1)\sin\theta_1 d\theta_1,\\
&\tilde{a}_{ns}(k_j)=\frac{d}{d\xi_0}j_n(\xi_0)\sum_{m=0}^{\infty}a_{ms}(k_j)B_{nm}(h_1),\quad j=1,3,\\
&\tilde{b}_{ns}(k_1)=4i\xi_0^3\sum_{p=0}^{\infty}\frac{d}{d\xi_0}j_p(\xi_0)R_{sp}(\theta_0)A_{np}(h_1)/(2p+1),\\
&\alpha_{n,s}(k_j)=\int_0^{\pi}\frac{d}{d\xi_j}j_n(\xi_j)P_n(\cos\theta_1)P_s(\cos\theta_1)\sin\theta_1 d\theta_1,\\
&\beta_{n,s}(k_1)=\int_0^{\pi}\frac{d}{d\xi_1}h_n^{(1)}(\xi_1)P_n(\cos\theta_1)P_s(\cos\theta_1)\sin\theta_1 d\theta_1,\\
&\tilde{\alpha}_{n,s}(k_j)=\int_0^{\pi}\frac{r'(\theta_1)}{r(\theta_1)^2}j_n(\xi_j)P_n^1(\cos\theta_1)P_s(\cos\theta_1)\sin\theta_1 d\theta_1,\\
&\tilde{\beta}_{n,s}(k_1)=\int_0^{\pi}\frac{r'(\theta_1)}{r(\theta_1)^2}h_n^{(1)}(\xi_1)P_n^1(\cos\theta_1)P_s(\cos\theta_1)\sin\theta_1 d\theta_1,\\
&A_{n,s}(k_j)=k_j\alpha_{n,s}(k_j)-\tilde{\alpha}_{n,s}(k_j),\quad B_{n,s}(k_1)=k_1\beta_{n,s}(k_1)-\tilde{\beta}_{n,s}(k_1),\\
&\tilde{A}_{n,s}(k_1)=\frac{d}{d\xi_0}j_n(\xi_0)\sum_{m=0}^{\infty}A_{ms}(k_1)B_{nm}(h_1).
\end{aligned}\right\}\qquad(30)$$

The infinite system (28) can be solved by the method of truncation [21].

5. Numerical experiments

Based on [23]:

$$\left.\begin{aligned} & h_n^{(1)}\left(kr_1\right)P_n\left(\cos\theta_1\right)=\sum_{p=0}^{\infty}\tilde{A}_{np}\left(h_1\right)h_p^{(1)}\left(kr\right)P_p\left(\cos\theta\right),\ r>h_1, \\ & \tilde{A}_{np}\left(h_1\right)=\sum_{\sigma=|p-n|}^{p+n}\left(2\sigma+1\right)i^{\sigma+p-n}\,b_p^{(n0\sigma0)}\,j_\sigma\left(kh_1\right) \end{aligned}\right\} \tag{31}$$

we present the function $p_2^{(2)}(r_1,\theta_1)$ in the coordinate system at the point O:

$$p_2^{(2)}\left(r,\,\theta\right)=P\sum_{n=0}^{\infty}N_n h_n^{(1)}\left(kr\right)P_n\left(\cos\theta\right),\quad N_n=\sum_{p=0}^{\infty}\tilde{A}_{pn}\left(h_1\right)y_p \tag{32}$$

Using the asymptotic expression for the function $h_n^{(1)}(kr)$ [21]:

$$h_n^{(1)}(kr)\approx\ (-i)^{n+1}e^{ikr}\,/\,kr,\quad kr\to\infty \tag{33}$$

we obtain the pressure in the far zone:

$$p_2(r,\theta)=P\frac{e^{ikr}}{kr}G(\theta)\,, \tag{34}$$

where

$$G(\theta)=\sum_{n=0}^{\infty}(-i)^{n+1}\left(X_n\frac{d}{d\xi_0}j_n\left(\xi_0\right)+f_n+\sum_{p=0}^{\infty}\tilde{A}_{pn}(h_1)y_p\right)P_n(\cos\theta)\,. \tag{35}$$

The unknown coefficients X_n, y_p are found from the system (29). Using Mathcad [24] the function G(θ) has been calculated for some parameters of the problem. The spherical functions have been calculated by means of built-in functions Mathcad. The infinite system (36) has been solved by the method of truncation [21]. The computational experiment showed that the truncation order for the considered parameters of the problem can be equal to 25. With this truncation the solution of the system (29) has accuracy 10^{-4}.

Figure 2 shows plots of function G(θ) for some values of the frequency f of the sound field. The remaining parameters are equal to: h_1 = 1.0 m, a = 0.3 m, b = 2a, d = 0.2 m, $\theta_0=\pi/4$. The areas D_1, D_2 are filled with water ($c_1=c_2$ = 1483 m/s, $\rho_1=\rho_2$ = 1000 kg/m^3). The area D_3 is filled with organic glass (c_3 = 2565 m/s, ρ_3 = 1200 kg/m^3).

Figure 3 shows plots of function G(θ) for some values of the angle θ_0 of the thin unclosed spherical shell Γ_1. The remaining parameters are equal to: $h_1 = 0.8$ m, $a = 0.3$ m, $b = 0.4$ m, $d = 0{,}1$ m, $f = 1000$ Hz. The areas D_1, D_2 are filled with water ($c_1 = c_2 = 1483$ m/s, $\rho_1 = \rho_2 = 1000$ kg/m^3). The area D_3 is filled with ice ($c_3 = 3980$ m/s, $\rho_3 = 900$ kg/m^3).

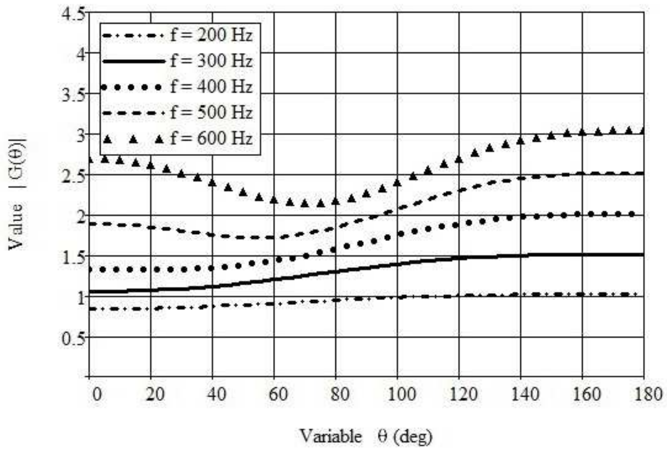

Fig. 2. Graphs of function G(θ) for some values of the frequency f of the sound field

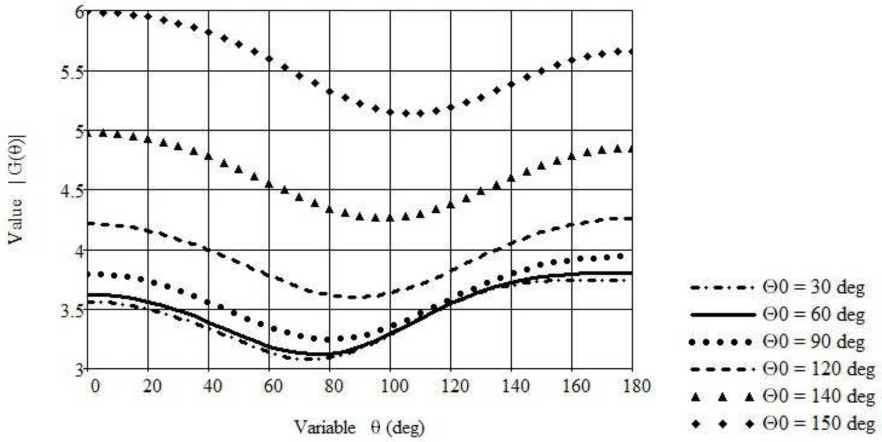

Fig. 3. Graphs of function G(θ) for some values of the angle θ_0

6. Conclusions

It has been shown that the solution of the problem of propagation of sound field by an unclosed spherical shell and a penetrable ellipsoid of rotation is reduced to the infinite system of linear algebraic equations of the second kind. The equation of spheroidal boundary is considered in the spherical coordinates. The spherical radiator is considered as the source of the sound field located within the thin unclosed spherical shell. The addition theorems for spherical wave functions and the method of solution of the dual series equations in Legendre's polynomials have been used. The developed methodology can be practically used in sound screen production.

Acknowledgment

The research leading to these results has supported by funding from the People Programme (Marie Curie International Research Staff Exchange) of the EU FP7/2007-2013/ under REA grant agreement n° PIRSES-GA-2013-610547.

References

[1] Blauert J., Xiang N.: Acoustics for Engineers, Springer-Verlag, Berlin, Heidelberg 2010.

[2] Fuchs H. V.: Applied Acoustics: Concepts, Absorbers, and Silencers for Acoustical Comfort and Noise Control, Springer-Verlag, Berlin, Heidelberg 2013.

[7] Erofeenko V.T., Demidchik V.I., Malyi S.V., Kornev R.V.: Penetration of electromagnetic waves through composite screens containing ideally conducting helices, J. Eng. Physics Thermophysics, 84 (2011) 799-806.

[4] Ivanov N.I.: Engineering acoustics. Theory and practice of noise control, Logos, Moscow 2008 (in Russian).

[5] Kleshchev A.A., Sheiba L.S.: Scattering of a sound wave by ideal prolate spheroids. Acoustic J., 16 (1970) 264-268 (in Russian).

[6] Sidman R.D.: Scattering of acoustical waves by a prolate spherical obstacle, J. Acoust. Soc. America, 52 (1972), 879-883.

[7] Abramov A.A., Dyshko A.L, Konyukhova N.B., Levitina T.V.: On a numerical-analytic investigation of problems of the diffraction of a plane sound wave by ideal prolate spheroids and triaxial ellipsoids, Comput. Math. Math. Phys., 35 (1995) 1103-1123

[8] Lauchle G.C.: Short-wavelength acoustic diffraction by prolate spheroids. J. Acoust. Soc. America, 58 (1975) 568-575.

[9] Germon A., Lauchle G.C.: Axisymmetric diffraction of spherical waves by a prolate spheroid, J. Acoust. Soc. America, 65 (1979) 1322-1327.

[10] Varadan V.K., Varadan V.V., Dragonette L.R., Flax L.: Computation of rigid body by prolate spheroids using the T-matrix approach, J. Acoust. Soc. America, 71 (1982) 22-25.

[11] Sammelmann G.S., Trivett D.H., Hackmann R.H.: High-frequency scattering from rigid prolate spheroids, J. Acoust. Soc. America, 83 (1988) 46-54.

[12] Barton J.P., Wolf N.L., Zhang H., Tarawneh C.: Near-field calculations for a rigid spheroid with an arbitrary incident acoustic field, J. Acoust. Soc. America, 103 (2003) 1266-1222.

[13] Burke J.E.: Scattering by penetrable spheroids, J. Acoust. Soc. America, 43 (1968) 871-875.

[14] Kotsis A.D., Roumeliotis J.A.: Acoustic scattering by a penetrable spheroid, Acoust. Phys., 54 (2008) 153-167.

[15] Kleshchev A.A., Rostovcev D.M.: Scattering of a sound by elastic and liquid ellipsoidal shells of revolution, Acoustic J., 32 (1986) 691-694 (in Russian).

[16] Kleshchev A. A.: With reference to low frequency resonances of elastic spheroidal bodies, J. Techn. Acoust., 2 (1995) 27-28.

[17] Bao X.L., Uberall H., Niemiec J.: Experimental study of sound scaterring by elastic spheroids, J. Acoust. Soc. America, 102 (1997), 933-942.

[18] Tolokonnikov L. A., Lobanov A. V.: About scattering of plane sound wave by inhomogeneous elastic spheroid, Proc. Tula State University, Natural Sciences, 3 (2011) 119-125 (in Russian).

[19] Tolokonnikov L. A.: Diffraction of plane sound wave on elastic spheroid with arbitrary located spherical vacuity, Proc. Tula State University, Natural Sciences, 2 (2011) 169-175 (in Russian).

[20] Grinchenko V.T., Vovk I.V., Matsipura V.T.: Fundamentals of acoustics, Naukova dumka, Kiev 2007 (in Russian).

[21] Ivanov E. A.: Diffraction of electromagnetic waves on two bodies, Springfield, Washington 1970.

[22] Shushkevich G.Ch., Kiselyova N.N.: Penetration of sound field through multilayered spherical shell, Computer Sci., 3 (2013) 47-57 (in Russian).

[23] Erofeenko V.T.: Addition theorems, Nauka and Technika, Minsk 1989.

[24] Shushkevich G.Ch., Shushkevich S.V.: Computer technology in mathematics, The system Mathcad 14: in 2 parts, Grevsova, Minsk 2012 (in Russian).

ROZCHODZENIE SIĘ FALI AKUSTYCZNEJ PRZEZ OTWARTĄ SFERYCZNĄ POWŁOKĘ ORAZ PRZENIKALNĄ ELIPSOIDĘ

Streszczenie

W artykule przedstawiono wynik rozwiązania problemu osiowosymetrycznego rozchodzenia się fali akustycznej przez otwartą sferyczną powłokę oraz przenikalną elipsoidę ruchu obrotowego. Sferyczny radiator, jako źródło pola akustycznego umieszczono w cienkiej sferycznej powłoce. Równanie granicy sferoidalnej podano we współrzędnych sferycznych. Pole rozproszonego ciśnienia wyrażono w funkcjach fal sferycznych. Wykorzystując odpowiednie dodatkowe twierdzenia rozwiązanie problemu wartości granicznej zredukowano do rozwiązania podwójnych równań w wielomianach Legendre'a, które przetworzono do systemu nieskończonego liniowych równań algebraicznych drugiego rodzaju. Otrzymano wzór do obliczenia pola przestrzennego oraz wyniki numeryczne dla różnych wartości parametrów.

Słowa kluczowe: pole akustyczne, powłoka sferyczna, elipsoida ruchu obrotowego, równania podwójne, radiator sferyczny

DOI: 10.7862/rm.2016.18

Otrzymano/received: 24.05.2016 r.
Zaakceptowano/accepted: 28.08.2016 r.

ZESZYTY NAUKOWE POLITECHNIKI RZESZOWSKIEJ 293, Mechanika 88
RUTMech, t. XXXIII, z. 88 (3/16), lipiec-wrzesień 2016, s. 233-245

Jana ŠUGÁROVÁ[1]
Martin FRNČÍK[2]
Martin NECPAL[3]
Jana MORAVČÍKOVÁ[4]
Martin KUSÝ[5]

EVALUATION OF TRIBOLOGICAL PROPERTIES OF LASER TEXTURED HARDENED TOOL STEELS

In this paper the laser surface texturing (LST) technology as one of the methods of tribological properties modifying of mating steel surfaces is analysed. The area density of dimple-like depression along with the dimple diameter are the only main factors which significantly influence the friction coefficient value, therefore the effect of different values of area density of dimples: 6 %, 11 % and 16 % on the contact coefficient of friction was analysed. Surface textures were manufactured on the planar areas of compression platens (90MnCrV8 tool steel) using a pulsed-beam laser. The values of coefficients of friction were obtained via a ring compression test. Test sample compression was realized in lubrication-free and hydrodynamic regime. A significant improvement of tribological properties in contact steel areas was experimentally observed in both friction regimes. The results of experiments showed that by applying of surface texturing with defined shape and dimensions of dimples and lubricating oil at the same time, the coefficient of friction value can be reduced to about of 75%.

Keywords: laser surface texturing (LST), tribological properties modification, coefficient of friction, ring compression test

1. Introduction

Laser surface texturing (LST) technology is a surface engineering process applied to improve surface tribological properties by production of regularly arranged microstructures on the contact surfaces of materials [1, 2]. Various

---

[1] Autor do korespondencji/corresponding author: Jana Šugárová, Slovak University of Technology, Faculty of Material Science and Technology, Bottova 25, 917 24 Trnava, Slovakia,e-mail: jana.sugarova@stuba.sk

[2-5] Martin Frnčík, Martin Necpal, Jana Moravčíková, Martin Kusý, Slovak University of Technology, Faculty of Material Science and Technology, Bottova 25, 917 24 Trnava, Slovakia, e-mails: martin.frncik@stuba.sk, martin.necpal@stuba.sk, jana.moravcikova@stuba.sk, martin.kusy@stuba.sk

types of surface patterns have been analyzed, but the dimples and grooves are the most widely used for laser textured tribo-surfaces [3, 4]. Surface texture can acts as lubricant reservoirs that can deliver the lubricant directly into the contact zone in starved oil lubrication [5, 8]. Another critical function of the textured surfaces is trapping of wear particles, because the elimination of wear particles from the contact interface reduces friction and wear in both lubricated and dry sliding regime [6, 9]. Furthermore, the textured surfaces can also increase load-carrying capacity [6, 7]. Laser surface texturing technology has been used in many technological fields to improve the tribological performances of contact surfaces, such as mechanical seals [10, 11], cutting tools [12-14], piston rings [15] and thrust bearing [16].

Dimple diameter, depth, and area density of dimples are the three major parameters of evenly distributed dimple patterns [17-19]. By considering all the geometric parameters, texture shapes are optimized to achieve the optimum shapes which will provide the best tribological performance in terms of minimum friction and maximum load carrying capacity [3]. Many researchers have contributed to the investigation on the influences of the above parameters on friction and load-carrying capacity of sliding surfaces [19, 20].

The area density of micro-dimples is another important parameter. In the works of Saeidi et al. [9] the effect of five chosen dimple parameters (depth, diameter, length, area density of dimples and sliding direction) has been analyzed. Authors found that the dimple diameter and the area density of dimples are the main factors which significantly influence the average coefficient of friction. For the tribo-pairs of metals lubricated by oil, several studies under controlled laboratory conditions have been performed in order to analyze the effect of area density of dimples on the coefficient of friction. Several experimental works show that the area density of dimples in the range of 5–13% is preferable for friction reduction, and the area density of dimples of above 20 % usually causes increasing the friction coefficient value [17, 21-23].

Many papers have examined the effect of dimple size, shape, and depth on friction reduction. No clear conclusions can be specified because there are additional factors influencing friction beside what were reported above (dimple size, shape, area density of dimples). Factors such as roughness of the non-textured surface area, pitch between dimples, uniformity of dimples, edge smoothness, dimple arrangement (pattern of dimple inside the contact), and the lack of control of dimple depths may all influence the friction phenomenon [24].

2. Experimental setup

This paper deals with the effect of different values of area density of dimples on the coefficient of friction value, which was measured at the tool–workpiece interface via a ring compression test. Each studied surface textures consist of dimple-like depressions with a diameter of 100±5 μm and a depth of 11 μm. Depressions are situated at the corners of the regular hexagon with a given side length in order to achieve the appropriate area density of dimples. One depression is placed into the centre of this pattern, as shown in figure 1. Three area densities of dimples have been experimentally studied:

- 6 %, depicted in figure 1a, with the hexagon side length of 0.389 mm,
- 11 %, depicted in figure 1b, with the hexagon side length of 0.287 mm,
- 16 %, depicted in figure 1c, with the hexagon side length of 0.238 mm.

Compression platens were made of 90MnCrV8 (according to EN ISO 4957) tool steel using turning technology. Chemical composition of used tool steel is specified in table 1. During the hardening process, which was carried out in the oil medium at the temperature of 770°C, the compression platens gained the required hardness of 58±1 HRC. Subsequently, the frontal surfaces of each platen were grinded to obtain a desired surface roughness Ra of 0.8 μm.

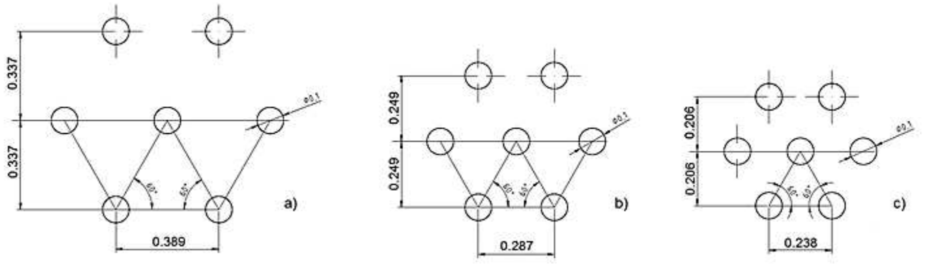

Fig. 1. Analysed surface textures with area density of dimples of 6 % (a), 11% (b) and 16% (c)

Table 1. Chemical composition of 90MnCrV8 tool steel (wt. %)

C	Si	Mn	P max	S max	Cr	V
0.91	0.10–0.40	1.90–2.10	0.030	0.030	0.20–0.50	0.05–0.15

Since there are strict dimensional and shape requirements for the texture dimples, it was necessary to experimentally define the optimal process parameters of laser beam, which will be subsequently used for production of various studied surface textures. For this purpose, a 3-level full factorial experiment has been carried out. Three laser texturing parameters as input factors were selected: laser beam repetition rate f_o, scanning speed v_s and laser track displacement Δ. The experimental factors and its levels are summarized in table 2.

During this experiment, testing cavities of square shape with dimensions of 5x5 mm were produced using specific combinations of input process parameters listed in table 2. Optimal process parameters (f_o, v_s and Δ) are that ones, which contributes to the finest machined surface roughness R_a. In this factorial design, a 5-axis high precision laser machining centre LASERTEC 80 SHAPE has been used for testing cavities production. This machine is equipped with a pulsed fiber Nd:YAG laser with a wavelength of 1064 nm. Laser beam power in each input parameter combination has been optimized in order to achieve the depth of cut of 1 μm per one layer. Surface roughness measurement of each testing cavity was realized using a Carl Zeiss Surfcom 5000 machine in two perpendicular directions (0° and 90°). Obtained surface roughness values from this experiment are listed in table 3.

Table 2. Factors and its levels

Factors	Factor levels		
	-1	0	+1
Repetition rate *f* (kHz)	50	75	100
Scanning speed v_s (mm·s-1)	1000	1300	1600
Tracks displacement *Δ* (μm)	5	10	15
Pulse duration time *t* (ns)	120		

Table 3. Parameters of laser beam utilized to production of micro-dimples and surface roughness of cavities

No.	*P*		f_o (kHz)	v_s (mm/s)	*Δ* (μm)	$Ra_{0°}$ (μm)	$Ra_{90°}$ (μm)	Ra_{av} (μm)
	(%)	*(W)*						
1.	15.30	7.96	50	1000	5	1.008	1.149	1.079
2.	19.50	10.14	50	1000	10	1.107	1.141	1.124
3.	23.0	11.96	50	1000	15	1.122	1.138	1.130
4.	17.50	9.10	50	1300	5	1.322	1.343	1.333
5.	21.0	10.92	50	1300	10	1.269	1.377	1.323
6.	25.50	13.26	50	1300	15	1.21	1.232	1.221
7.	18.0	9.36	50	1600	5	1.316	1.283	1.300
8.	23.0	11.96	50	1600	10	1.237	1.279	1.258
9.	27.80	14.46	50	1600	15	1.481	1.476	1.479
10.	17.30	13.84	75	1000	5	0.907	1.013	0.960
11.	23.50	18.80	75	1000	10	0.999	1.108	1.054
12.	27.20	21.76	75	1000	15	1.124	1.166	1.145
13.	**20.50**	**16.40**	**75**	**1300**	**5**	**0.956**	**0.962**	**0.959**
14.	26.50	21.20	75	1300	10	1.021	1.189	1.105
15.	30.80	24.64	75	1300	15	1.105	1.187	1.146
16.	21.80	17.44	75	1600	5	0.996	1.131	1.064
17.	28.0	22.40	75	1600	10	1.16	1.179	1.170
18.	33.50	26.80	75	1600	15	1.194	1.154	1.174
19.	17.0	17.0	100	1000	5	0.90	1.033	0.967
20.	23.50	23.50	100	1000	10	0.971	1.05	1.011
21.	27.50	27.50	100	1000	15	1.194	1.245	1.220
22.	20.0	20.0	100	1300	5	0.993	1.108	1.051
23.	26.0	26.0	100	1300	10	1.034	1.069	1.052
24.	30.0	30.0	100	1300	15	1.223	1.229	1.226
25.	22.0	22.0	100	1600	5	0.985	1.12	1.053
26.	28.50	28.50	100	1600	10	1.108	1.201	1.155
27.	33.80	33.80	100	1600	15	1.107	1.173	1.140

Table 3 summarizes a design of the experiment including three input factors and three levels (3^3 full factorial experiment, 27 runs). An optimised laser beam power (*P*) for all runs is also stated in this table. Average machined surface roughness represents the desired response, which was measured in all combination of input parameters. It can be seen, that in run no. 13 the average machined surface roughness reached the lowest value from the all test runs. This is the reason why this combination of laser beam process parameters was chosen as the optimal for following production of surface textures on the planar surfaces of the compression platens.

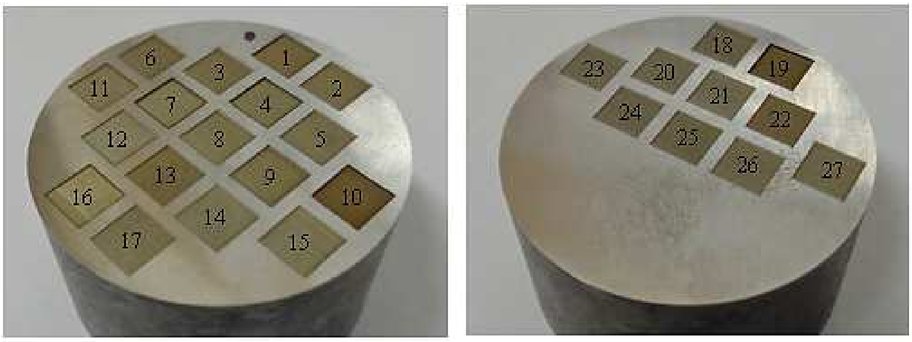

Fig. 2. Testing cavities manufactured in 3^3 full factorial experiment

Figure 2 demonstrates the produced testing cavities. The surface colour variation is a result of various laser pulse energies. Figure 3 shows the real surface of the testing cavity produced under laser beam parameters: power = 16.4 W, repetition rate = 75 kHz, laser scanning speed = 1300 $\text{mm}\cdot\text{s}^{-1}$ and laser tracks distance = 5 μm (run no. 13).

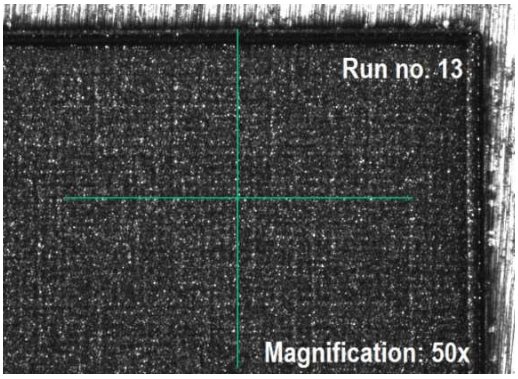

Fig. 3. Testing cavity with the finest machined surface roughness (Ra = 0.959 μm)

Surface textures production on the planar surfaces of compression platens has been carried out using the same laser machine, and optimal process parameters (run no. 13). Each surface texture was manufactured on the area of circle with a diameter of 16 mm (area of 201 mm^2). Figure 4 shows the textures produced on the planar surfaces of the compression platens using a material ablation process. Production times for three different sample textures are listed in table 4.

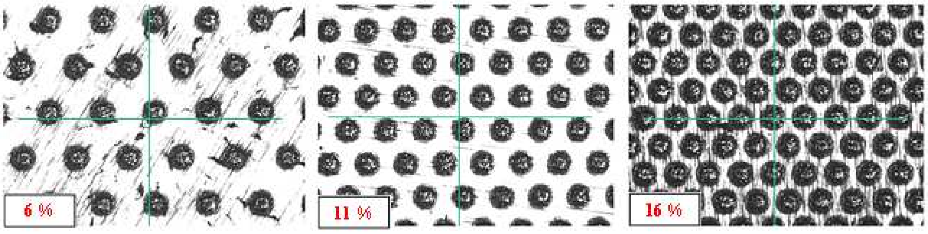

Fig. 4. Textures on the planar surfaces of compression platens produced using LST technology

Table 4. Production time of surface textures

Area density of dimples	Number of depressions	Production time for one platen
6 %	1522	15 min 41 s
11 %	2772	22 min 45 s
16 %	4070	30 min 47 s

Shape and dimensional characteristics of produced surface texture dimples have been carried out using laser confocal microscope Zeiss LSM 700 (with the resolution of 10 nm). Overall shape and dimensions (diameter and depth) of chosen dimple of each studied texture were analyzed. Based on this analysis it can be concluded, that all chosen dimples meet the desired characteristics. Figure 5 represents the real 3D dimple shape of surface texture with area density of dimples of 6 %. Dimensional characteristics are: a dimple diameter of 98 μm and a depth of 11 μm, dimple volume of about 39 122 μm^3. This figure also shows that around the edge of depression a rim of solidified melt was created (average rim height is 6.1 μm and a width of about 20 μm, rim volume is equal to 74 553 μm^3). This rim is a typical element of the depressions manufactured by laser beam in material ablation processes. It has been experimentally demonstrated that these solidified melted rims around the edges of depressions have a negative effect on the tribological performance of contacting surfaces [21]. Therefore, to remove the rims formed in material ablation process all textured surfaces of all compression platens were polished with the polycrystalline diamond suspension (grain size of 1 μm, polishing time of 35 s) using a Jeanwirtz TF250 polishing machine. The platens were subsequently cleaned in an ultrasonic bath in acetone medium in order to any polishing suspension or polishing debris were removed from the depressions (bath time of 30 s).

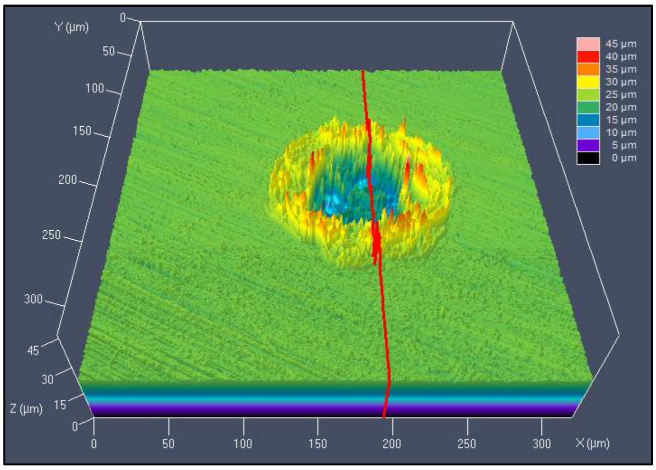

Fig. 5. Real 3D shape of selected depression of texture with area density of dimples of 6 %

A ring compression test was performed in order to determine the coefficient of friction values of the contact pairs. During this test, a ring-shaped test sample is axially compressed between the pair of textured compression platens. Test samples were manufactured of low carbon steel by turning technology. Frontal surfaces of test samples were non-textured. These surfaces have been grinded to obtain a required surface roughness (Ra) of 0.4 µm. Table 5 shows the chemical composition of test samples material. The ring compression test is based on the assumption that the coefficient of friction is constant at the whole contact surface and the deformation of the test ring is homogeneous. During the compression, the hole diameter of the test sample can be reduced, remain constant or even increased (depending on the value of the coefficient of friction). When the test sample is compressed in frictionless conditions, the hole diameter increases proportionally with the increase of the outer diameter. With the friction coefficient increasing the increase of the hole diameter is hampered and at a certain value of radial pressure this diameter can be reduced [25]. The ratio of outer diameter to the hole diameter to the height of test sample $D : d : h$ is equal to 6 : 3 : 2. The dimensions of test samples are typically 12 mm : 6 mm : 4 mm according to this ratio. It is important to preserve approximately an equal compression of the test sample ΔH during the test. This value should be within the range of 0.2 to 0.5 mm. Ring compression test has been performed using an universal forming machine EU40; the strain rate was set up to the 10^{-4} s^{-1} value.

Table 5. Chemical composition of test samples material (wt. %)

C_{max}	P_{max}	S_{max}	N_{max}
0.17	0.045	0.045	0.007

Table 6. Selected physical and chemical properties of applied Renep CGLP 220 high performance slideway oil [26]

Property	Value
Viscosity at 40 °C (mm^2/s)	220 (DIN EN ISO 3104)
Density at 15 °C (kg/m^3)	895 (DIN 51 757)
Flash point (°C)	240 (ISO 2592)
Friction coefficient (-)	0.145

Based on the deformation of the sample hole and the sample strain, coefficient of friction values can be simply defined for each compression. Coefficient of friction evaluation was performed in lubrication-free (dry contact) and hydrodynamic regimes at the room temperature of 21°C. Both non-textured and textured compression platens were tested in these lubrication regimes for comparison. Three test samples were gradually compressed in each combination of surface texture and friction regime, subsequently the average value of coefficient of friction was calculated for each compression situation. To ensure the hydrodynamic regime (“full lubrication” configuration) the oil-based liquid lubricant Renep CGLP 220 was used. Physical and chemical properties of applied lubricant are depicted in table 6.

3. Results and discussion

The average values of coefficient of friction evaluated based on the ring compression are summarized in table 7. Graphical comparison of these values is depicted in figure 6. According to the ring compression test, the reference value of the friction coefficient for non-textured compression platens (in lubrication-free regime) achieves the value of 0.258. The coefficient of friction value for steel – steel contact pair should be within the range of 0.25 to 0.8 [27]. It was experimentally confirmed, that the coefficient of friction value for non-textured steel surfaces tested with the oil lubricant is 0.157. This value is slightly higher than the value specified by the oil producer. This means that by using only the oil lubricant for modification of the tribological conditions of the mating surfaces, the coefficient of friction value can be reduced by 39.14%.

Table 7. Values of friction coefficient obtained via ring compression test

Compression platen surface	Friction coefficient (-)	
	lubrication-free regime	hydrodynamic regime
Non-textured	0.258±0.013	0.157±0.0080
Textured (6 %)	0.137±0,007	0.069±0.0010
Textured (11 %)	0.198±0.016	0.116±0.0035
Textured (16 %)	0.254±0.005	0.128±0.0065

A blue line in the figure 6 represents the coefficient of friction value evaluated using only the surface texturing for modification of tribological properties. The lowest value of the coefficient of friction was achieved using the surface texture with the area density of dimples of 6%. The coefficient of friction reaches the value of 0.137, which means that its value was reduced nearly to the half of its original value (46.90% reduction). The reason for this fact is that the contact area between the compression tools and test sample was sufficiently reduced which resulted in lower forming pressures and forces. Higher values of area density of dimples contribute to an increase in value of the coefficient of friction. This relation has strong linear character. Surface texture with area density of dimples of 16% reaches the coefficient of friction value of 0.254, which is almost the same value as the reference (1.55% friction reduction). In this case, the surface texture does not contribute to friction reduction, because the space between the each dimple start acting like a peak of material, which makes the flow of test sample material more difficult during the deformation process. The friction coefficient value in lubrication-free regime can be evaluated from the following equation:

$$f = 0.0117\, S_p + 0.0676 \tag{1}$$

where, f is the coefficient of friction (-) and S_p is the area density of dimples (%). The value of a coefficient of determination is 0.99. So, 99% of the variability in the response can be explained by the linear regression model.

A yellow line in the figure 6 represents the coefficient of friction value evaluated for the surface textures with the various densities and with the application of oil lubricant. The coefficient of friction value increases from the value of 0.069 to 0.128 with the increasing the value of the area density of dimples and similarly to the previous case, the relationship is linear. Combination of area density of 6% together with the oil lubricant contribute to the lowest value of coefficient of friction (0.069). In this case, compared to the non-textured surfaces with no lubricant and the non-textured surfaces with oil lubricant it was found that the reduction in the coefficient of friction value is equal to 73.26 and 56.05%, respectively. There are two reasons why the coefficient of friction reaches a low value in these cases: (a) surface texture reduced the contact area between the test sample and compression platens and, (b) micro-dimples act as a micro-reservoir for liquid lubricant.

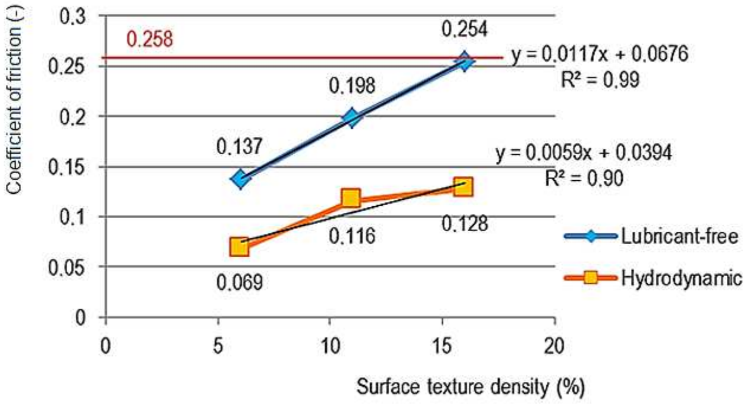

Fig. 6. Coefficient of friction value vs. the surface texture density

According to the [28] the most important surface texture parameter is the ratio of the dimple height to the dimple diameter. According to the Ronen et al. [29] this ratio value should be within the range of 0.1 to 0.2 in order to ensure the friction reduction in hydrodynamic lubrication regime. In this paper, the value of this ratio is 0.112. Therefore, the coefficient of friction value reduction is so significant. The coefficient of friction value in hydrodynamic lubrication regime can be evaluated from the following equation:

$$f = 0.0059\, S_p + 0.0394 \tag{2}$$

where, the f is the coefficient of friction (-) and S_p is the area density of dimples (%). The value of a coefficient of determination is 0.90. So, 90% of the variability in the response can be explained by the linear regression model.

4. Conclusion

Laser surface texturing technology is a widely used method to improve the load capacity, the wear resistance, and the friction coefficient of tribological components. To analyse the influence of laser texturing on the coefficient of friction measured at the tool – workpiece interface a dimple-like depressions with a depth of 11 μm, a diameter of 98 μm and a texture densities of 6%, 11% and 16% has been formed in the planar areas of compression platens made of 90MnCrV8 steel. Laser texturing has been carried out using a pulsed fiber Nd:YAG laser with power of 16.4 W, repetition rate of 75 KHz and laser track displacement of 5 μm. The morphological characterization of manufactured dimples has been performed using a laser confocal microscope. Tribological tests have been carried out in two different lubrication regimes, i.e. lubricant-free and hydrodynamic, where oil lubricant with viscosity of 220 $mm^2 \cdot s^{-1}$ was used at room temperature.

Experimental results showed a significant improvement of friction behaviour under hydrodynamic conditions. Textured contact surface with the area density of dimples of 6% modified by oil lubricant showed the best friction behaviour compared to the reference value. Reference value of the coefficient of friction, corresponding to a non-textured surface, was established at a value of 0.258. In this case, the coefficient of friction value was reduced to a value of 0.069 (73.26% reduction in value), which means, that surface texturing with defined and suitable shape and dimensions of dimples, and using an appropriate liquid lubricant at the same time, the value of coefficient of friction can be reduced to about of 75%. A similar improvement of friction behaviour using a surface texture was observed in lubrication-free regime too. Surface texture with dimple density of 6% contributed to friction reduction to about of 46.9%. Increasing of coefficient of friction with the increase of dimple density was observed in both friction regimes; these functionalities have strong linear character.

The surface texturing is an important process in reducing friction and wear. The reduction of contact area, the function of micro-trap for wear debris, and the micro-reservoirs for lubricant retention are the main mechanisms responsible for reducing the friction and wear in laser surface texturing.

Acknowledgement

This research work was supported by an international research project under the MANUNET 2014 call, entitled: Innovative methods of sheet metal forming tools surfaces improvement – R&D (2014/11283); VEGA project called: Laser surface texturing technology research for an optimizing of tribological conditions in the sheet metal forming processes (1/0669/15). The authors would also like to thank for financial contribution from the SUT Grant scheme for Support of Young Researchers (1350/16).

References

[1] Wang Z. et al.: Angle-dependent lubricated tribological properties of stainless steel by femtosecond laser surface texturing, Optics Laser Technol., 81 (2016) 60-66.

[2] Etsion I.: State of the art in Laser surface texturing, J., Tribology, 127 (2005) 248-253.

[3] Ibatan T. et. al.: Recent development on surface texturing in enhancing tribological performance of bearing sliders, Surface Coatings Technol., 272 (2015) 102-120.

[4] Yan J. et. al.: Fabricating micro-structured surface by using single-crystalline diamond endmill, Int. J. And. Manuf. Technol., 51 (2010) 957-964.

[5] Vilhena L. M. et. al.: Surface texturing by pulsed Nd:YAG laser, Tribology Int., 42 (2009) 1496-1504.

[6] Gualtieri E. et. al.: Increasing nanohardness and reducing friction of nitride steel by laser surface texturing, Tribology Int., 42 (2009) 699-705.

[7] Shinkarenko A. et al.: The effect of surface texturing in soft elasto-hydrodynamic lubrication, Tribology Int., 42 (2009) 284-292.

[8] Fowell M. et al.: Entrainment and inlet suction: Two mechanisms of hydrodynamic lubrication in textured bearings, J. Tribology, 129 (2007) 336-347.

[9] Saeidi F. et al.: Effect of surface texturing on cast iron reciprocating against steel under starved lubrication conditions: A parametric study, Wear, 348-349 (2016) 17-26.

[10] Wan Y. and Xiong D.-S.: The effect of laser surface texturing on frictional performance of face seal, J. Mat. Proc. Technol., 197 (2008) 96-100.

[11] Feldman Y. et al.: A hydrostatic laser surface textured gas seal, Tribology Letters, 22 (2006) 21-28.

[12] Walter C. et. al.: Laser-structured grinding tools- Generation of prototype patterns and performance evaluation, J. Mat. Proc. Technol., 214 (2014) 951-961.

[13] Dumitru G. et al.: Laser processing of hardmetals: Physical basics and applications. Int. J. Refractory Metals Hard Mat., 23 (2005) 278 – 286.

[14] Kümmel J. et al.: Study on micro texturing of uncoated cemented carbide cutting tools for wear improvement and built-up edge stabilization, Journal of Materials Processing Technology, 215 (2015) 62-70.

[15] Ryk G., Etsion I.: Testing piston rings with partial laser surface texturing for friction reduction, Wear, 261 (2006) 792-796.

[16] Brizmer V. et. al.: A laser surface textured parallel thrust bearing, Tribology transactions, 46 (2003) 397-403.

[17] Yan D. et. al.: Significance of dimple parameters on the friction of sliding surfaces investigated by orthogonal experiments, Tribology Trans., 53 (2010) 703-712.

[18] Ma Ch., Zhu H.: An optimum design model for textured surface with elliptical-shape dimples under hydrodynamic lubrication, Tribology Int., 44 (2011) 987-995.

[19] Wang X. et. al.: Design principles for the area density of dimple patterns, J. Eng. Tribology, 229 (2015) 538-546.

[20] Galda L. et. al.: Dimples shape and distribution effect on characteristics of Stribeck curve, Tribology Int., 42 (2009) 1505-1512.

[21] Kovalchenko A. et. al.: The effect of laser surface texturing on transitions in lubrication regimes during unidirectional sliding contact, Tribology Int., 38 (2005) 219-225.

[22] Ryk G. et. al.: Experimental investigation of laser surface texturing for reciprocating automotive components, Tribology Trans., 45 (2002) 444-449.

[23] Grabon W. et. al.: Improving tribological behaviour of piston ring–cylinder liner frictional pair by liner surface texturing, Tribology Int., 61 (2013) 102-108.

[24] Hsu S. M. et. al., Friction reduction using discrete surface textures: principle and design, J. Physics D: Applied Physics, 47 (2014) 335307.

[25] Plančak M. et. al.: Possibilities to measure contact friction in bulk metal forming, Tehnički vjesnik, 19 (2012) 727-734.

[26] Renep CGLP, 2013, Fuchs product information, online: <http://www3.ikaros.net/datablad/pblad/smorjmedel%20(Univar)/600631321_Renep_CGLP_PBLAD.

[27] The Engineering ToolBox, 2014, Friction and coefficients of friction, online: <http://www.engineeringtoolbox.com/friction-coefficients-d_778.

[28] Shinkarenko A. et. al.: Theoretical analysis of surface-textured elastomer sleeve in lubricated rotary sliding, Tribology Trans., 53 (2010) 376-385.

[29] Ronen A. et. al.: Friction-reducing surface-texturing in reciprocating automotive components, Tribology Trans., 44 (2001) 359-366.

OCENA WŁAŚCIWOŚCI TRIBOLOGICZNYCH HARTOWANYCH STALI NARZĘDZIOWYCH TEKSTUROWANYCH LASEROWO

Streszczenie

W artykule przedstawiono analizę technologii laserowego teksturowania powierzchni (LTP) jako jedną z metod modyfikacji właściwości tribologicznych współpracujących powierzchni stalowych. Podstawowy szyk tekstury powierzchni składa się z wgłębień o zakrzywionym dnie, które są umieszczone w narożach sześciokąta foremnego. Dodatkowo jedno zagłębienie jest umieszczone w środku szyku. Parametry zagłębień są następujące: średnica 100±5 μm, głębokość 11 μm, stosunek głębokości do średnicy 0,11. Gęstość powierzchniowa wgłębień oraz średnica wgłębienia są głównymi czynnikami, które w sposób istotny wpływają na wyjściową wartość współczynnik tarcia, dlatego analizowano wpływ różnych wartości gęstości powierzchniowej wgłębień, tj. 6%, 11% i 16% na wartość kontaktowego współczynnika tarcia. Tekstury powierzchni zostały utworzone na płaskich powierzchniach płyt dociskowych (stal narzędziowa 90MnCrV8) za pomocą wiązki pulsacyjnej lasera. Wartości współczynników tarcia otrzymano za pomocą testu ściskania pierścienia. Próbki do badań ze stali węglowej S235JRG1 były ściskane osiowo pomiędzy parą teksturowanych płyt dociskowych. Ściskanie badanej próbki zostało zrealizowane w warunkach braku smarowania oraz smarowania hydrodynamicznego. Wyniki doświadczalne wykazały, że przez zastosowanie teksturowania powierzchni o określonym kształcie i wymiarach wgłębień oraz ciekłego smaru, wartość współczynnika tarcia może być zmniejszona prawie o 75%.

Słowa kluczowe: teksturowanie laserowe powierzchni (TLP), modyfikacja właściwości tribologicznych, współczynnik tarcia, test ściskania pierścienia

DOI: 10.7862/rm.2016.19

Otrzymano/received: 30.05.2016 r.
Zaakceptowano/accepted: 12.09.2016 r.

ZESZYTY NAUKOWE POLITECHNIKI RZESZOWSKIEJ 293, Mechanika 88
RUTMech, t. XXXIII, z. 88 (3/16), lipiec-wrzesień 2016, s. 247-258

Tomasz TRZEPIECIŃSKI[1]
Romuald FEJKIEL[2]
Andrzej KUBIT[3]
Wojciech BOCHNOWSKI[4]

EVALUATION OF FRICTION COEFFICIENT OF AN AUTO-BODY STEEL SHEET

In this paper the results of strip drawing tests aimed to determine the friction coefficient in sheet metal forming operations are presented. The tests were conducted using a specially designed tribological simulator. The deep drawing quality steel sheet used in the automotive industry was tested. The relationship that shows the effect of sheet normal load, tool surface roughness, lubrication conditions and sample orientation according the rolling direction of the sheet on the value of friction coefficient are presented and discussed. The Scanning Electron Microscope (SEM) micrographs of sheet surfaces after the friction test allowed us to identify the mechanisms that occur at the contact of two bodies with rough surfaces. The results of the tests indicate that the relationship between friction force and normal force is nonlinear. Thus, the value of the friction coefficient is changed with the change of the load value.

Keywords: coefficient of friction, friction, strip-drawing test, surface roughness

1. Introduction

Sheet metal forming is one of the most popular methods of preparing finished products in the automotive industry. The protective coating is sometimes applied as the last stage of the operation and requires an appropriate surface roughness of a drawpiece. Friction forces have a significant influence on the distribution and the value of strains and thus the quality of the product. The most important factors that determine obtaining a high quality product is the size of the thinning walls. Non-heterogeneity of the drawpiece deformation is

---

[1] Autor do korespondencji/corresponding author: Tomasz Trzepieciński, Rzeszow University of Technology, Al. Powstańców Warszawy 12, 35-959 Rzeszów, Poland, tel. 17 8651714, e-mail: tomtrz@prz.edu.pl

[2] Andrzej Kubit, Rzeszow University of Technology, e-mail: akubit@prz.edu.pl

[3] Romulad Fejkiel, State School of Higher Vocational Education, Krosno, e-mail: rfejkiel@wp.pl

[4] Wojciech Bochnowski, University of Rzeszow, Rzeszów, e-mail: wobochno@ur.edu.pl

mainly conditioned by the presence of friction forces at the interface of the deformed material and tools.

The processes taking place in the contact zone are affected by many factors, including by the size of normal pressure, material and surface topography, sheets, tools and lubricant, among others. The factors that depend on the forming process include the value of normal pressure and speed of deformation. The correct selection of the values of process parameters determines obtaining a product of desired dimensional and shape quality. The role and effects of the occurrence of frictional resistance are difficult to define. The unfavourable effects of the presence of frictional resistance include, among others [1-3]: non-heterogeneity of drawpiece deformation, an increase of the pressure exerted by the punch causing a danger of crack occurrence, as well as the worsening of the surface quality of a drawpiece. Beneficial effects of the frictional resistance on the forming process may include friction existing between the sheet metal and the punch because it increases the permissible value for the maximum force in deep-drawing. Disadvantageous phenomenon of friction can be counteracted through the use of appropriate lubricants and an increase in the hardness of tools.

The main factors influencing the tribological phenomena in plastic working processes include macro- and microgeometry of contacts, the kinematics of the tool, physical and chemical phenomena at the contact surface and the temperature [1, 4, 5]. Physical and chemical phenomena occurring in the contact zone depend, among others things, on the materials of the frictional pair and the chemical affinity of the materials in contact. During the sheet metal formation frictional connections are created using metallic dyes that are destroyed during the friction process [6, 7]. The value of the frictional resistance essentially depends on the shear strength of frictional connections. The effects of contact pressure and sliding velocity under mixed lubrication based on a friction testing of steel sheet was investigated by Tamai et al. [8]. A proposed new nonlinear friction coefficient model allows us to evaluate the change in the friction coefficient during continuous sliding and predictions of the friction coefficient were extremely accurate in comparison with the conventional methods.

In the processes of sheet metal forming using rigid tools, macro- and microgeometry contact friction pairs have a significant impact on the amount of frictional resistance. Generally, the friction is due to the ploughing effect between asperities [9] and adhesion between contacting asperities [10]. The three dominating fattening mechanisms during sheet forming are: flattening due to sliding, flattening due to normal load and flattening due to normal loading. Flattening increases the real area of contact, resulting in a higher value of friction coefficient [10]. Asperity flattening due to combined normal loading and deformation of the underlying bulk material is described in a flattening model proposed by Wasteneng [11]. Surface changes due to asperity deformations influence the load-carrying capacity of the lubricant [12]. Ma et al. [13] calculated the asperity flattening in metal forming and showed that the area of contact ratio increased as a function of normal pressure. Furthermore the relative sliding between a tool and a sheet can increase the area of the contact ratio. As the lubricant viscosity becomes lower, the friction coefficient is higher [14].

Methods such as strip drawing testing [15], draw bead testing [16], bending under tension testing [17], strip reduction testing [18] and testing using slider-on-sheet tribometer [19] are widely used to estimate the frictional resistance and wear behaviour between rough surfaces. Tisza and Fülöp [20] classified friction tests for sheet metal forming as a function of the main performed operations: stretch drawing, stretch forming and deep drawing. The stretch-drawing type tests are widely used to investigate the effect of several material and technological parameters on frictional resistances [21, 22]. Significant advances regarding friction behaviours in plastic forming were summarised by Wang et al. [23, 24] from four aspects, namely, friction testing, characterising, modelling and controlling.

The strip drawing test is one of the simplest tribological tests to determine the friction coefficient in sheet metal forming. This paper presents the results of the strip drawing test aim to determine the friction coefficient of deep drawing quality steel sheet used in the automotive industry. Several relationships that illustrate the effect of sheet metal surface roughness, lubrication conditions and sheet orientation on the value of the friction coefficient are presented and discussed.

2. Material and method

The friction tests were conducted by strip drawing tests in which the flat sample was placed between two fixed cylindrical rolls with equal radii (Fig. 1). The test was carried out in such a way that a strip of the sheet was clamped with specified force between two cylindrical rolls of equal radii of 20 mm. The values of both forces, the normal force F_N and the pulling force F_P, were constantly recorded using electric resistance strain gauge technique, 8-channel universal amplifier of HBM's QuantumX data acquisition system and computer PC. The specimens for the friction tests were made of deep-drawing quality 1 mm thick 09J steel sheet used in the automotive industry. According to the standard PN-EN 10130+A1:1999 the tested steel sheet with drawing category SB is intended for hard to form drawpieces with complex shapes. The samples were prepared as a strip with a width of 20 mm and a length of about 200 mm, cut along the rolling direction of the sheet. The rolls were made of cold working tool steel. The tests were performed under the following conditions:

- surface roughness of rolls was measured along the generating line of rolls: 0.63 and 1.25 µm,
- clamping force: 0.6, 1.05, 1.45 and 1.85 kN,

- lubrication conditions: dry friction and lubrication using machine oil LAN-46.

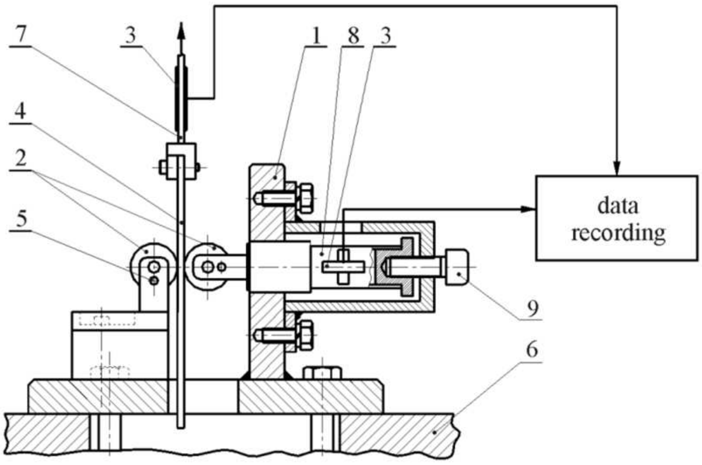

Fig. 1. Scheme of measuring device: 1 – frame; 2 – working rolls; 3 – load cells; 4 – specimen; 5 – blocked pin; 6 – grip of testing machine; 7, 8 – tension members; 9 – set bolt.

During the recording of the pulling and clamping forces, the sheet was drawn for a distance of about 10 mm. Next, the clamping force value was increased simultaneously during the tests.

The mean value of the friction coefficient, μ, was determined according to the equation (1) for the stabilised range of values of F_P and F_N. The coefficient of friction is evaluated separately for all levels of variation of clamping force (f in figure 2). For these ranges we received about 120-160 values of the coefficient of friction (range μ_i in figure 2). So it was assumed that such number of the values of the coefficient of friction is sufficient to evaluate the average coefficient of friction representative for analysed lubrication conditions.

$$\mu = \frac{F_P}{2 \cdot F_N} \tag{1}$$

where: F_P – pulling force, F_N – clamping force.

To realise dry conditions both rolls and sheet specimens were degreased using acetone.

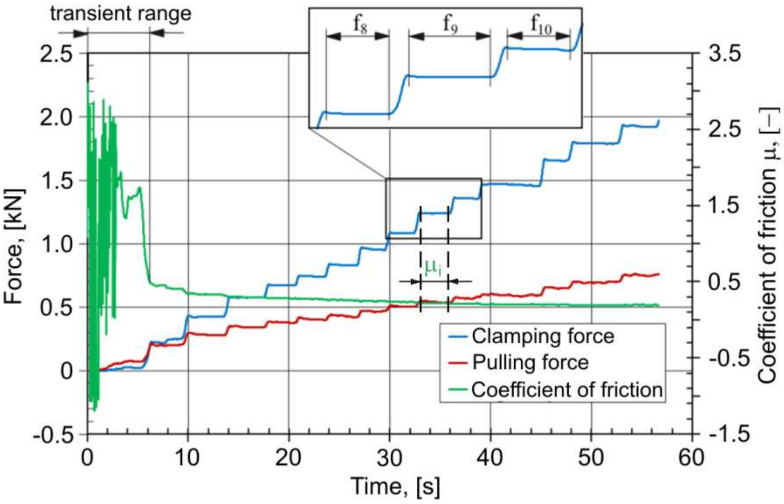

Fig. 2. Exemplary plot of variation of values of clamping force F_N and pulling force F_T versus specimen displacement

To study the effect of sample strain on the change of the surface topography and friction coefficient the samples were straightened using the uniaxial tensile test to receive different strain values logarithmic strain ε_l: 0.095, 0.14 and 0.182.

To determine the mechanical properties (Table 1), the tensile test was carried out in the universal testing machine. Surface roughness 3D parameters of the sheets (Table 2) were measured by using Taylor Hobson Surtronic 3+ instrument. It was assumed that one measurement is representative to characterize the sheet surface roughness. Table 1 presents the mechanical properties and selected spatial parameters of the sheets.

Table 1. Basic mechanical parameters of tested sheet

Sample orientation	Yield stress $R_{p0,2}$ MPa	Ultimate strength R_m MPa	Elongation A_{50}	Strain hardening coefficient C MPa	Strain hardening exponent n
0°	162	310	0.42	554	0.21
90°	163	312	0.41	530	0.21

Table 2. Selected roughness parameters of tested sheet

Measurement orientation according to sheet rolling direction	Surface roughness parameters					
	Ra, μm	Rq, μm	Rt, μm	Rp, μm	Rsk	Rz, μm
0º	1.4	1.68	9.6	5.8	0.36	9.4
90º	1.74	1.92	10.1	6.2	0.14	8.7

3. Results and discussion

The change of the contact surface is accompanied by a continuous change in the geometry of the contact. The values of arithmetical mean deviation of the surface roughness profile Ra (Fig. 3a) and maximum height of the roughness profile Rz (Fig. 3b) increase with the sample pre-strain value. For both measurement orientations, according to the sheet rolling direction, this tendency is similar. The sample pre-strain causes not only the change of the surface topography but also, by strain hardening phenomena, changes the mechanical parameters of the surface asperities. An increase of maximum height of the roughness profile does not increase the frictional resistances. The strain-hardened asperities are less susceptible to the flattening process, which causes the intensification of surface mechanical wear.

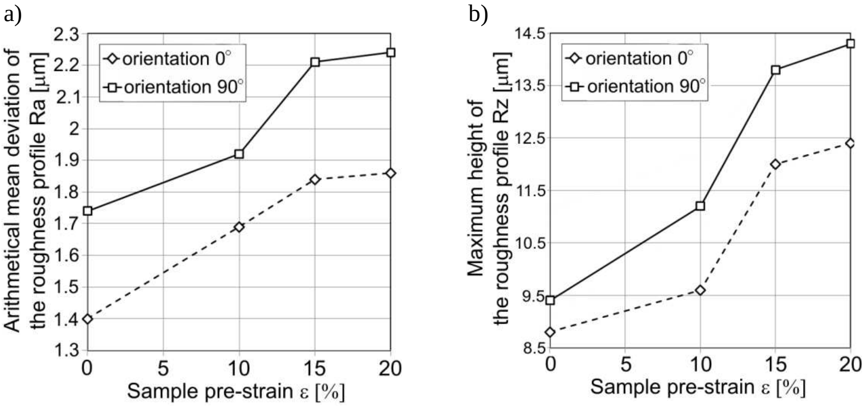

Fig. 3. Effect of sample pre-strain value on variation of the roughness parameters Ra (a) and Rz (b)

The width of the sample changes with an increase of the sample pre-strain value. However, according to the Coulomb model of friction the value of the friction coefficient does not depend on the contact area. It allows one to compare the values of the friction coefficients determined for different sample pre-strains. The value of the friction coefficient decreases as the clamping force increases for both dry (Fig. 4) and lubricated conditions (Fig. 5). It can be concluded that the relationship between the normal force and friction force is nonlinear. In consequence the coefficient of friction value changes with the change of load. This relationship is also observed in other recent studies [2].

In general, at low values of load the coefficient of the friction value increases with the load and after reaching a certain value of load the value of friction coefficient rapidly decreases in the case of metals with a small capacity for strain-hardening. In the case of metals with a high capacity for strain hardening, the friction coefficient value is almost constant [3].

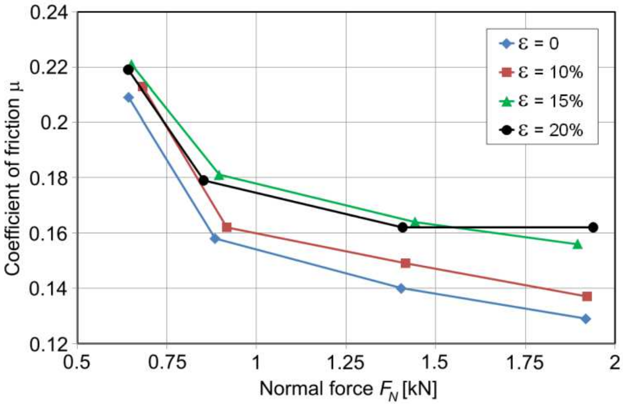

Fig. 4. Relation of friction coefficient value versus normal force F_N determined by using rolls with surface roughness Ra = 0.63 μm in dry friction condition

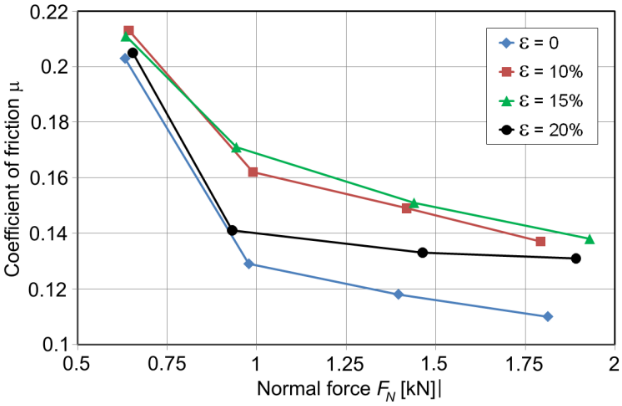

Fig. 5. Relation of friction coefficient value versus normal force F_N determined by using rolls with surface roughness Ra = 0.63 μm in lubricated condition

The increasing of a samples' pre-strain value causes an increase in the coefficient of the friction value. However, character of this relationship depends on the friction conditions. In both friction conditions the fast decrease of the friction coefficient is observed in the case of normal loads less than about 1 kN. After exceeding this value of normal load the intensity of decreasing friction coefficient is smaller. Roughening of asperities, observed during testing the sheets at normal load value exceeding 1 kN, tends to decrease the real area of contact resulting in a lower coefficient of friction. The samples pre-strained to 15 and 20% exhibit the highest and similar coefficient of friction values but only in the case of dry friction. The small difference in the value of the coefficient of friction determined for both dry and lubricated conditions, especially in the case of small values of normal force can be a result of a dominant influence both of flattening and ploughing mechanisms on the value of the coefficient of friction. The surface roughness valleys are too small to supply effectively lubricant to asperity contact area.

The evaluation of the average normal force $F_N^{(av)}$ for all tests performed at similar value of normal load allows us to make a generalised qualitative assessment of the effect of normal load on the coefficient of the friction value. An increase of normal load value causes a decrease of the coefficient of friction value (Fig. 6). For all used levels of normal load, the sample pre-strain at 10% increases the friction coefficient value in comparison to the test of original sheet surface. Further increase of sample pre-strain causes a decrease of the friction coefficient value. This relation depends on the ratio of frictional resistances at boundary lubrication regime and flattening mechanism.

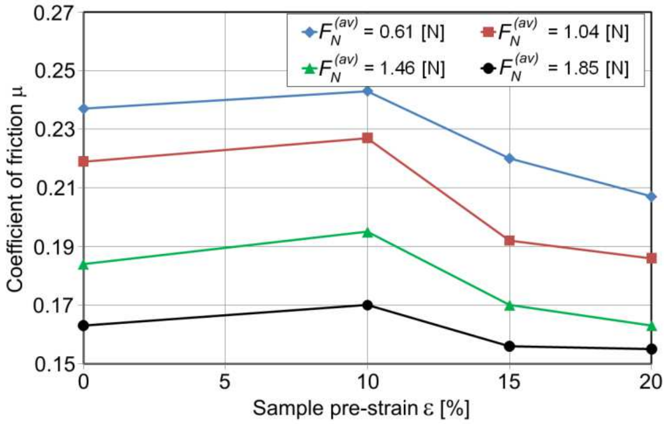

Fig. 6. Relation of friction coefficient value versus sample pre-strain determined by using rolls with surface roughness Ra = 1.25 μm in lubricated condition

In the case of the highest pre-strain value (20%) the lubrication of the contact surface causes the coefficient of friction to be smaller than in the case of pre-strains 10 and 15%. This can be explained by the fact that roughness valleys act as oil reservoirs (Fig. 7b). The profile height of samples pre-strained at 10 and 15% is not able to supply the suitable oil volume and the mechanism of surface roughness flattening (Fig. 7c) dominates. The phenomenon of flattening causes an increase in the real contact area. The increase in the real contact area occurs gradually from the initial peak surface roughness contact to full contact after balancing normal force and the force required to deform roughness [2].

In the boundary lubrication regime, friction is mainly described by adhesion and ploughing between contacting asperities. The intensification of the ploughing mechanism is observed mainly in the case of dry friction conditions (Fig. 7c) rather than in lubricated conditions (Fig. 7d).

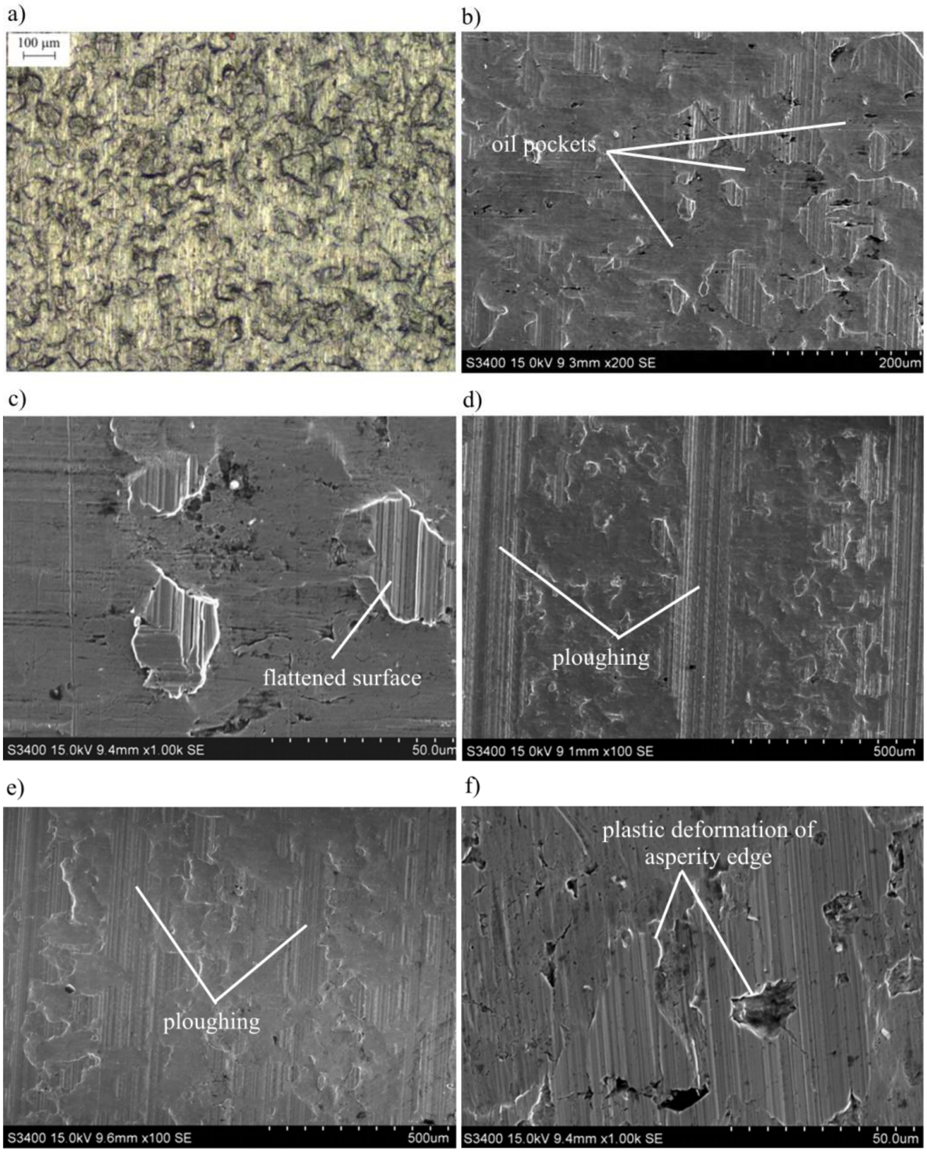

Fig. 7. View of original surface of tested steel sheet (a) and Scanning Electron Microscope micrographs of tested sheets: oil reservoirs (b), flattened asperities (c), ploughed surface observed in dry (d) and lubricated surfaces (e), and plastic deformation of the asperities edge

4. Summary and conclusions

Initially during sheet metal forming there is little real contact area. The surfaces adhere to each other only at the asperities, which are then deformed plastically until the contact surface becomes sufficient to transfer the load under the action of pressure. One of the main mechanisms during sheet forming is flattening and elastic-plastic deformation of surface asperities. It causes an increase of the real area of contact, which leads to an increase of the shear stress during the movement of the contacted surfaces. Conducted investigations of frictional resistance of auto-body steel sheets allow us to conclude that:

- the values of arithmetical mean deviation of the surface roughness profile and maximum height of the roughness profile increase with the sample pre-strain value,
- the dominant contact mechanism in the case of dry friction is asperity flattening,
- the value of the friction coefficient decreases as the clamping force increases for both dry and lubricated conditions,
- the relation between the normal force and friction force is nonlinear.

References

[1] Fratini L., Lo Casto S., Lo Valvo E.: A technical note on an experimental device to measure friction coefficient in sheet metal forming, J. Mat. Proc. Technol., 172 (2006) 16-21.

[2] Trzepieciński T., Bazan A., Lemu H.G.: Frictional characteristics of steel sheets used in automotive industry, Inte. J. Automotive Technol., 16 (2015) 849-863.

[3] Gierzyńska M.: Tarcie, zużycie i smarowanie w obróbce plastycznej metali, WNT, Warszawa 1983.

[4] Trzepieciński T.: Badanie właściwości tarciowych blach stalowych dla przemysłu motoryzacyjnego, Hutnik, 81 (2014) 446-449.

[5] Wang W., Zhao Y., Wang Z., Hua M., Wei X.: A study on variable friction model in sheet metal forming with advanced high strength steels, Tribology Int., 93 (2016) 17-28.

[6] Kirkhorn L., Bushlya V., Anderson M., Ståhl J-E.: The influence of tool steel microstructure on friction in sheet metal forming, Wear, 302 (2013) 1268-1278.

[7] Neale M.J.: The tribology handbook. Second edition, Butterworth Heinemann, Oxford 2001.

[8] Tamai Y., Inazumi T., Manabe K.: FE forming analysis with nonlinear friction coefficient model considering contact pressure, sliding velocity and sliding length, J. Mat. Proc. Technol., 227 (2016) 161-168.

[9] Wilson W.: Friction models for metal forming in the boundary lubrication regime, ASME, 10 (1988) 13-23.

[10] Hol J., Cid Alfaro M.V., de Rooij M.B., Meinders T.: Advanced friction modeling for sheet metal forming, Wear, 286-287 (2012) 66-78.

[11] Wasteneng J.D.: Modeling of contact and friction in deep drawing processes, Ph.D. Thesis, University of Twente, 2001.

[12] Hol J., Meinders V.T., Geijselaers H.J.M., van den Boogaard A.H.: Multi-scale friction modeling for sheet metal forming: The mixed lubrication regime, Tribology Int., 85 (2015) 10-25.

[13] Ma B., Tieu A.K., Lu C., Jiang Z.: A finite-element simulation of asperity flattening in metal forming, J. Mat. Proc. Technol., 130 (2002) 450-455.

[14] Lee B.H., Keum Y.T., Wagoner R.H.: Modeling of the friction caused by lubrication and surface roughness in sheet metal forming, J. Mat. Proc. Technol., 130-131 (2002) 60-63.

[15] Kirkhorn L., Frogner K., Andersson M., Ståhl J.E.: Improved tribotesting for sheet metal forming, Procedia CIRP, 3 (2012) 507-512.

[16] Trzepieciński T., Lemu H.G.: Study on frictional conditions of AA5251 aluminium alloy sheets using drawbead simulator test and numerical methods, Strojniski Vestnik - J. Mech. Eng., 60 (2014) 51-60.

[17] Lemu H.G., Trzepieciński T.: Numerical and experimental study of the frictional behaviour in bending under tension test, Strojniski Vestnik - J. Mech. Eng., 59 (2013) 41-49.

[18] Andreasen J.L., Bay N., Andersen M., Christensen E., Bjerrum N.: Screening the performance of lubricants for the ironing of stainless steel with a strip reduction test, Wear, 207 (1997)1-5.

[19] van der Heide E., Huis in 't Veld A.J., Schipper D.J.: The effect of lubricant selection on galling in a model wear test, Wear, 251 (2001) 973-979.

[20] Tisza M., Fülöp T., A general overview of tribology of sheet metal forming, J. Technol. Plasticity, 26 (2001) 11-25.

[21] Wiklund D., Rosén B-G., Wihlborg A.: A friction model evaluated with results from a bending-under-tension test, Tribology Int., 42 (2009) 1448-1452.

[22] Azushima A., Sakuramoto M.: Effects of plastic strain on surface roughness and coefficient of friction in tension-bending test, CIRP Annals – Manuf. Technol., 55 (2006) 303-306.

[23] Wang D., Yang H., Li H.: Advance and trend of friction study in plastic forming, Trans. Nonferrous Metals Soc. China, 24 (2014) 1463-1272.

[24] Wang D., Li H., Ma J., Li G.: Tribological evaluation of surface modified H13 tool steel in warm forming of Ti-6Al-4V titanium alloy sheet, Chinese J. Aeronautics, 27 (2014) 1002-1009.

WYZNACZANIE WSPÓŁCZYNNNIKA TARCIA STALOWEJ BLACHY KAROSERYJNEJ

Streszczenie

W artykule przedstawiono wyniki testów przeciągania pasa blachy mających na celu określenie wartości współczynnika tarcia w procesach kształtowania blach. Badania przeprowadzono za pomocą specjalnie zaprojektowanego symulatora tribologicznego. Badaniom poddano blachę stalową głębokotłoczną wykorzystywaną w przemyśle motoryzacyjnym. Przedstawiono i omówiono zależności pomiędzy siłą nacisku, chropowatością powierzchni narzędzia, warunkami tarcia oraz orientacją próbki względem kierunku walcowania a wartością współczynnika tarcia. Zdjęcia SEM (Scanning Electron Microscopy) powierzchni blach po procesie tarcia pozwoliły na rozpoznanie mechanizmów tarcia występujących podczas kontaktu dwóch ciał o powierzchni chropowatej. Wyniki badań wskazały, że zależność pomiędzy siłą tarcia i siłą normalną jest nieliniowa, dlatego wartość współczynnika tarcia zmienia się wraz ze zmianą wartości obciążenia.

Słowa kluczowe: współczynnik tarcia, tarcie, test przeciągania pasa blachy, chropowatość powierzchni

DOI: 10.7862/rm.2016.20

Otrzymano/received: 21.08.2016 r.
Zaakceptowano/accepted: 16.09.2016 r.

ZESZYTY NAUKOWE POLITECHNIKI RZESZOWSKIEJ 293, Mechanika 88
RUTMech, t. XXXIII, z. 88 (3/16), lipiec-wrzesień 2016, s. 259-266

Ján VIŇÁŠ[1]
Ľuboš KAŠČÁK[2]

ANALYSIS OF WELDABILITY OF DUAL-PHASE STEEL USED IN AUTOMOTIVE INDUSTRY

This paper deals with the problems of weldability of high strength dual-phase steel sheets used in the car body production. The properties of the joints made by resistance spot welding (RSW) and laser welding were analysed. The two grades of dual-phase steels such as DP 600 and DP 800 were used. The joints were made by overlapping of two sheets in the method 21 according to EN ISO 4063 (RSW), and as butt weld without a gap by laser welding (method 52 in EN ISO 4063). The parameters of RSW and laser welding were chosen according to the recommendations of IIW. The quality of welded joints was evaluated by visual control, static tension test, and a microstructural analysis of the joints on the light microscopy.

Keywords: spot welding, laser welding, dual-phase steel

1. Introduction

The production of automobiles in the EU significantly increases in recent years. Increasing the production leads to the application of new advanced materials in order to minimize the costs of production, as well as to produce fuel-efficient and ecological products, enhancing comfort and security of car passengers. The car producers also utilize the various combinations of materials, such as most used steel sheets of drawing grade quality as well as advanced high-strength steel sheets (AHSS) or high-strength low alloy (HSLA) steels [1, 2]. It is necessary not only to produce car body parts but to join them into a complex structure as well. Mainly resistance spot welding and laser welding are the joining method used to join thin-walled assemblies in automotive industry. Therefore, the research into weldability of these materials is important, especially optimization of welding properties. The galvanized steel sheets with corrosion resistance have been used in automobile industry, replacing cold rolled steel sheets as auto body materials to improve the corrosion resistance

---

[1] Autor do korespondencji/corresponding author: Ján Viňáš, Technical University of Košice, Letná 9, 042 00 Košice, Slovakia, e-mail: jan.vinas@tuke.sk

[2] Ľuboš Kaščák, Technical University of Košice, Slovakia e-mail: lubos.kascak@tuke.sk

and overall service life of vehicles [3, 4]. Advanced high-strength steels for automotive applications have been the aim of research and the development in the recent years. Their introduction in car bodies allows to reduce their weight and improve the car safety. Nevertheless, the weldability of AHSS is an important issue since cars typically contain thousands of spot welds [5, 6]. Ferrite-martensite dual-phase (DP) steels are some of the most common AHSSs, which are currently used in automotive industry. Their microstructure offers a suitable combination of strength and formability. The term dual-phase steel refers to the predominance of two lattices, the body-centered-cubic (bcc) ferrite and the relatively harder body-centered-tetragonal (bct) martensite. These two lattices are produced by some annealing in the range of the upper (A_3) and lower (A_1) transformation temperatures, where austenite and ferrite are formed, and a subsequent rapid cooling where the austenite is eventually transformed into martensite [7, 8].

The paper deals with the analysis of possibility of welding of high-strength dual-phase steels sheets DP600 and DP 800 by resistance spot welding and laser welding.

2. Experimental procedure

Within the experimental work, the welded samples were prepared in the laboratory using the two most commonly used method of welding in automotive industry. The first method of joining was resistance spot welding, carried out on the programmable pneumatic welding machine BPK 20 with welding electrode tips of ø5 mm. An influence of welding current as the main parameter of resistance spot welding on the quality of spot welds was observed. The spot weld was made by overlapping of the steel sheets in position PA according to EN ISO 6947 standard. The second method of joining was laser welding using CO_2 AF8P laser with maximum output of 8 kW. The samples were welded along the sheet width (800 mm) in position PA according to EN ISO 6947 standard without a gap between the sheets.

Two types of high-strength dual-phase steel sheets DP600 and DP800. These steel sheets with the thickness of 0.8 mm were hot-dip galvanized. The chemical composition and basic mechanical properties of the welded material are shown in table 1 and table 2, respectively. For each type of welding, five samples were prepared for static tensile test and two samples for metallographic analysis. Labelling of samples was as follows:

- samples A and B: steel sheet DP600 made by resistance spot welding,
- samples C and D: steel sheet DP800 made by resistance spot welding,
- sample E: steel sheet DP600 made by laser welding,
- sample F: steel sheet DP800 made by laser welding.

Table 1. Chemical composition of welded steel sheets (wt-%)

DP 600	C	Mn	Si	P	S	Al	Cu	Cr
	0.111	1.963	0.279	0.026	< 0.002	0.031	0.019	0.206
	Mo	Ni	V	Ti	Nb	Co	W	Fe
	< 0.002	< 0.002	0.012	< 0.002	0.020	0.017	0.005	Bal
DP 800	C	Mn	Si	P	S	Al	Cu	Cr
	0.062	1.623	0.036	0.022	< 0.002	0.086	0.119	0.247
	Mo	Ni	V	Ti	Nb	Co	W	Fe
	0.293	0.107	0.056	< 0.002	0.077	0.1	< 0.002	Bal

Table 2. Basic mechanical properties of welded materials given by producer

Material	Yield stress R_e MPa	Ultimate strength R_m MPa	Total elongation A_5 %
DP 600	300 - 470	580 - 670	26
DP 800	450 - 560	780 - 900	17

The following parameters of resistance spot welding were used:

- pressing force of welding electrodes: Fz = 4 kN,
- welding time: T = 20 periods (1 period = 0.02 s),
- welding current: I = 4.5 kA for samples A and C,
  I = 7kA for samples B and D.

The following parameters were used for laser welding:

- output: P = 1700 W,
- laser mode: TEM 10 - Gauss,
- gas: Ar 12 l/min,
- welding speed: v_z = 2000 mm/min,
- beam focusing: on the top sheet surface f = 0÷0.5 mm,
- wave-length: λ = 10.6 μm.

The quality of the welds was evaluated by the visual observation according to EN ISO 17637 recommendations. Furthermore, two different destructive tests of the welds were carried out. The spot welded joints were tested in static tensile test according to STN EN 05 1122 standard. The welded joints were tested in a tensile test in transverse direction according to STN EN ISO 4136 standard. The influence of parameters on the microstructure changes in the welded metal and heat-affected zone (HAZ) was evaluated with the light microscopy using metallographic samples prepared according to EN ISO 17639 standard.

3. Results and discussion

The analysis of the quality of welded joints by visual test has not proved the presence of external surface defects on the spot welds. Similarly, the absence of pores, cracks and other defects was observed in laser welds. The welds can be classified on the basis of a visual test. The maximum load-bearing capacity of the welded joints and the place of destruction were evaluated by a tensile test. When using the welding current I = 4.5 kA in joining DP600 steels, the average load-bearing capacity of the spot welds was 8300 N. Increasing the welding current to the value of I = 7 kA led to increasing the average load-bearing capacity of the joints to the value of 9150 N. The average value of load-bearing capacity of the spot welded DP800 steels using welding current I = 4.5 kA was 8670 N. Even in these steels the higher average value of load-bearing capacity of 9430 N was measured when welding current was increased to I = 7 kA, as shown in table 3.

Table 3. The average values of load-bearing capacity F_{max}, R_e and R_m of welded joints (BM - Base Metal, HAZ – Heat-Affected Zone, WM - Weld Metal, FW - Fusion Weld)

Sample	F_{max}, N	Type of joint	Destruction
A	8300	FW	HAZ
B	9150	FW	HAZ
C	8670	FW	HAZ
D	9430	FW	HAZ
Sample	**R_e, MPa**	**R_m, MPa**	**Destruction**
E	372	620	BM
F	467	788	BM

The measured values of R_e and R_m in laser welds of both dual-phase steel sheets (Table 3) exceeded the minimum values of the base material declared by the sheet producer (Table 2). In the tensile test, the destruction of the joints occurred outside the laser weld, in the base material. The minimum measured average value of R_m in the case of the sample E made of DP600 steel sheets was 620 MPa and in the case of the sample F made of DP800 steel sheets was 788 MPa. The results of the macroscopic analysis are presented in figures 1-4. No presence of cavities and pores in the weld nugget was observed in the samples A and C (Figs. 1 and 3) made by resistance spot welding. Increasing the welding current led to the changes in dimensions of the weld nugget, heat affected zone as well as the occurrence of cavities in the middle of the weld nugget (Figs. 2 and 4). The typical dendritic growth of weld metal was observed on weld structures. In the weld metal of laser welded samples in both DP600 and DP800 steel sheets no internal defects were observed (Fig. 5). The microstructure of the sample A with the transition of base metal via heat-affected zone to the weld nugget is shown in Fig. 6. The changes in grain size , the orientation of grains and phase were observed. It was found that a multi-phase structure is composed of fine-grained martensite, bainite and ferrite. Figure 7 shows a cavity in the middle of the weld nugget of the sample D, which occurred due to shrinkage of weld metal during the solidification process.

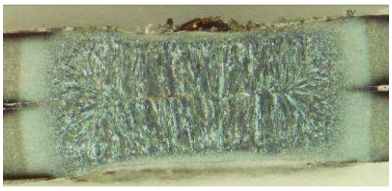

Fig. 1 Macrostructure of sample A (DP 600)

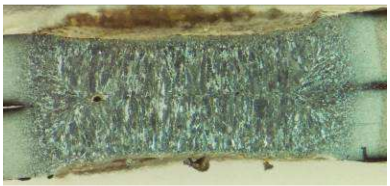

Fig. 2 Macrostructure of sample B (DP 600)

Fig. 3 Macrostructure of sample C (DP 800)

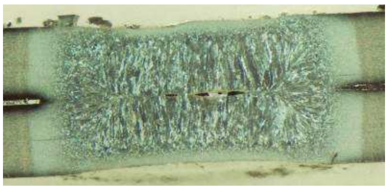

Fig. 4 Macrostructure of sample D (DP 800)

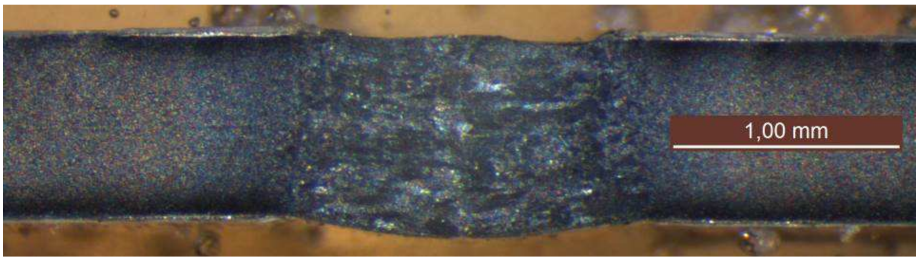

Fig. 5. Laser weld of DP 600

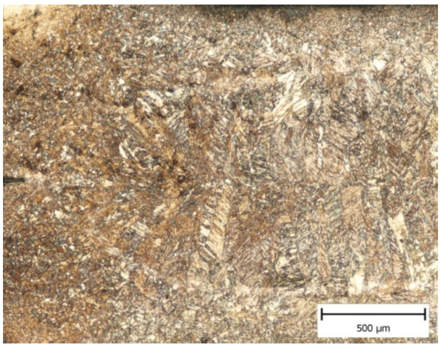

Fig. 6 Weld microstructure of sample A (DP 600)

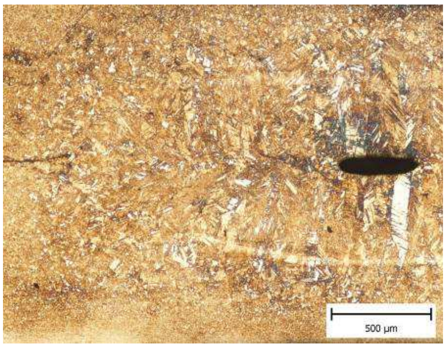

Fig. 7 Weld microstructure of sample D (DP 800)

The microstructure of the base material of both DP600 (Fig. 8) and DP800 steels is composed by ferritic matrix with dispersed fine-grained martensite. The microstructure of HAZ of lase welds of DP800 steel (Fig. 9) is composed of multiphase microstructure of fine-grained martensite and bainite in the ferritic matrix. Concerning the used welding parameters and the thickness of the sheets the width of the HAZ in both materials was the same. The microstructure of weld metal of laser welds (Fig. 10) is composed primarily of the coarse-grained lamellar martensite and bainite due to rapid cooling.

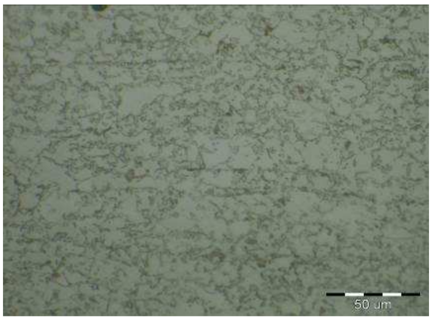

Fig. 8. Base material of DP 600

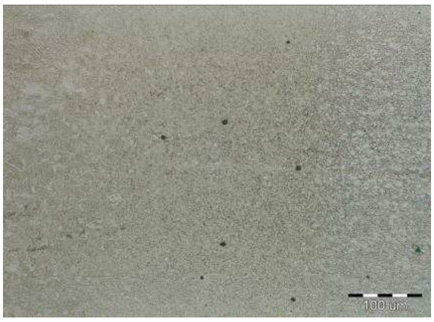

Fig. 9. Microstructure of HAZ of sample F

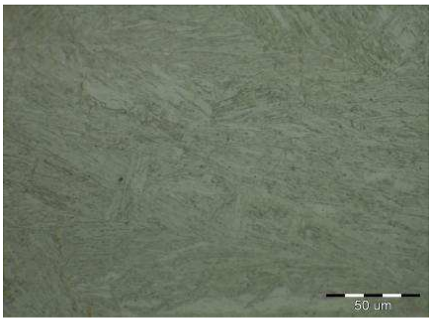

Fig. 10. Microstructure of laser weld metal of sample F

4. Conclusions

The application of high-strength steels in car body production is still increasing because of weight reduction of cars. Development of the construction of laser welders and the reducing economic demands of the welding process is increasingly attractive to the producers. On the other hand, these progressive high-speed welding methods require optimization of welding parameters, especially in welding of difficult to weld materials. The methods also require the application of accurate fixtures ensuring the correct position of the narrow welds, which is common problem in the industry.

The resistance spot welding of dual-phase steel sheets requires consistent optimization of welding parameters. When using 20 periods of welding time, it is suitable to use low values of welding current (4.5 kA), since no internal defects occur in welding nugget and load-bearing capacity of the joints is sufficient.

The laser welding is a suitable method for joining the dual-phase high-strength steel sheets. Since the weld and heat-affected zone are narrow, no internal defects occur in the weld metal and the load-bearing capacity of the joints is high considering the predominant martensitic microstructure. The load-capacity of laser weld joint is higher than the ultimate tensile strength of welded materials.

Acknowledgement

This work was supported by the Slovak Research and Development Agency under the contract No. APVV-0273-12.

References

[1] Mucha J., Kaščák Ľ., Spišák E.: The experimental analysis of forming and strength of Clinch Riveting sheet metal joint made of different materials, Adv. Mech. Eng., 59 (2013) 1-11.

[2] Zhang X., Chen G., Zhang Y., Lai X.: Improvement of resistance spot weldability for dual-phase (DP600) steels using servo gun, J. Mat. Proc. Technol., 209 (2009) 2671-2675.

[3] Hernandez V.H.B., Panda S.K., Okita Y., Zhou N.Y.: A study on heat affected zone softening in resistance spot welded dual phase steel by nanoindentation, J. Mat. Sci., 45 (2010) 1638-1647.

[4] Kaščák Ľ., Brezinová J., Mucha J.: Evaluation of corrosion resistance of galvanized steel sheets used in automotive production, Mat. Sci. Forum, 818 (2015) 141-144.

[5] Dancette S., Fabregue D., Estevez R., Massardier V., Dupuy T., Bouzekri M.: A finite element model for the prediction of Advanced High Strength Steel spot welds fracture, Eng. Fracture Mech., 87 (2012) 48-61.

[6] Kaščák Ľ., Spišák E., Gajdoš I.: Influence of welding parameters on the quality of resistance spot welded joints of DP600 steels, Key Eng. Mat., 635 (2015) 143-146.

[7] Pouranvari M., Marashi S.P.H., Jaber H.L.: DP780 dual-phase-steel spot welds: critical fusion-zone size ensuring the pull-out failure mode, Mat. Technol., 49 (2015) 579-585.

[8] Lifang M., Jiming Y., Dongbing Y., Jinwu L., Genyu C.: Comparative study on CO_2 laser overlap welding and resistance spot welding for galvanized steel, Mat. Design, 40 (2012) 433-442.

ANALIZA ZGRZEWALNOŚCI STALI DWUFAZOWEJ STOSOWANEJ W PRZEMYŚLE MOTORYZACYJNYM

Streszczenie

Artykuł jest poświęcony problemom zgrzewalności wysokowytrzymałych dwufazowych blach stalowych stosowanych do produkcji karoserii samochodowych. Analizowano właściwości połączeń wykonanych metodami punktowego zgrzewania oporowego (PZO) oraz spawania laserowego. Badania przeprowadzono dla dwóch gatunków blach dwufazowych tj. DP600 oraz DP800. Połączenia zakładkowe blach wykonano zgodnie z metodą 21 ujętą w normie EN ISO 4063. Podczas spawania laserowego blachy łączono metodą na styk bez szczeliny (metoda 52 zgodnie z normą EN ISO 4063). Parametry zgrzewania punktowego oraz spawania laserowego były zgodne z wytycznymi IIW. Ocenę jakości wykonanych połączeń przeprowadzono na podstawie kontroli wzrokowej, statycznego testu rozciągania oraz analizy mikrostrukturalnej połączeń z wykorzystaniem mikroskopii świetlnej.

Słowa kluczowe: zgrzewanie punktowe, spawanie laserowe, stal dwufazowa

DOI: 10.7862/rm.2016.21

Otrzymano/received: 29.05.2016 r.
Zaakceptowano/accepted: 11.09.2016 r.

Informacje dodatkowe

1. Lista recenzentów współpracujących będzie opublikowana w czwartym numerze *Zeszytów Naukowych Politechniki Rzeszowskiej, Mechanika*, z. 88 (4/2016) oraz zamieszczona na stronie internetowej:

   http://oficyna.portal.prz.edu.pl/pl/zeszyty-naukowe/mechanika/

2. Zasady recenzowania są udostępnione na stronie internetowej:

   http://oficyna.portal.prz.edu.pl/zasady-recenzowania/

3. Informacje dla autorów artykułów są udostępnione na stronie internetowej:

   http://oficyna.portal.prz.edu.pl/informacje-dla-autorow/

4. Formularz recenzji jest udostępniony na stronie internetowej:

   http://oficyna.portal.prz.edu.pl/pl/zeszyty-naukowe/mechanika/

5. Instrukcja dla autorów omawiająca szczegółowo strukturę artykułu, jego układ, sposób przygotowywania materiału ilustracyjnego i piśmiennictwa jest zamieszczona na stronach internetowych:

   http://oficyna.portal.prz.edu.pl/pl/instrukcja-dla-autorow/

   oraz

   http://oficyna.portal.prz.edu.pl/pl/zeszyty-naukowe/mechanika/

   w zakładce „Instrukcja dla autorów".

6. Dane kontaktowe do redakcji czasopisma, adresy pocztowe i e-mail do przesłania artykułów oraz dane kontaktowe do wydawcy są podane na stronie internetowej (Komitet Redakcyjny):

   http://oficyna.portal.prz.edu.pl/pl/zeszyty-naukowe/mechanika/

Zasady recenzowania, informacje dla autorów, formularz recenzji, instrukcja dla autorów i dane kontaktowe do redakcji czasopisma i wydawcy będą opublikowane w czwartym numerze *Zeszytów Naukowych Politechniki Rzeszowskiej, Mechanika*, z. 88 (4/2016).

Nakład 200 egz. Ark. wyd. 4,73. Ark. druk. 5,25. Papier offset. 80g B1.
Oddano do druku we wrześniu 2016 r. Wydrukowano we wrześniu 2016 r.
Drukarnia Oficyny Wydawniczej, al. Powstańców Warszawy 12, 35-959 Rzeszów
Zam. nr 96/16